

2.07 Fission Product Chemistry in Oxide Fuels[☆]

Markus H.A. Piro, Ontario Tech University, Oshawa, ON, Canada and Canadian Nuclear Laboratories, Chalk River, ON, Canada

Jean-Christophe Dumas, CEA, DES, IRESNE, DEC, Cadarache F-13108, Saint-Paul-Lez-Durance, France

Brent J Lewis and William T Thompson, Royal Military College of Canada, Kingston, ON, Canada

Fernando C Iglesias, Kinectrics, Toronto, ON, Canada

© 2020 Elsevier Ltd. All rights reserved.

2.07.1	Introduction	173
2.07.1.1	General Characteristics of Thermal and Fast Reactor Fuels	175
2.07.1.1.1	Plutonium distribution	175
2.07.1.1.2	Radial dependence of fuel stoichiometry after irradiation	176
2.07.1.2	Fission Product Classifications in Irradiated Fuels	176
2.07.2	Chemical State of Fission Products in Irradiated Oxide Fuels	180
2.07.2.1	Volatile Fission Products	181
2.07.2.2	Distribution and Segregation of Fission Products	182
2.07.2.3	Reaction of Fission Products With Zirconium Alloy Cladding	182
2.07.2.4	Oxygen in Zirconium Alloy cladding	182
2.07.3	Thermodynamic Modeling of Oxide Fuels	183
2.07.3.1	Uranium–Oxygen Binary System	183
2.07.3.2	Phase Diagram Studies of Fission Products in Oxide Fuels	184
2.07.3.2.1	Solutes in UO ₂	185
2.07.3.2.2	Noble metals	187
2.07.3.2.3	Non-fluorite oxide phases	187
2.07.3.2.4	Other metallic phases (UPd ₃ –URh ₃ –URu ₃)	188
2.07.3.2.5	Establishing the fuel inventory for equilibrium calculations	189
2.07.3.2.6	Irradiated fuel system	189
2.07.4	Defective Fuel Behavior	192
2.07.4.1	Fuel Oxidation Phenomena	192
2.07.4.2	Aqueous Fuel and Fission Product Behavior	192
2.07.5	High-Temperature Fuel and Fission Product Behavior Under Accident Conditions	194
2.07.6	Conclusion	197
References		197

Abbreviations

CANDU Canada deuterium uranium	NRA nuclear reaction analysis
CEA Commissariat à l’Énergie Atomique et aux énergies alternatives	ORNL Oak Ridge National Laboratory
EAC environmental-assisted corrosion	PBF power burst facility
ERD elastic recoil detection	PIXE particle-induced X-ray emission
FBR fast breeder reactor	PWR pressurized water reactor
FLHT full-length high temperature	SCC stress corrosion cracking
FP fission product	SFD severe fuel damage
FPT fission product tests	ST source term
HI horizontal induction	STEP source term experiments project
JAEA Japan Atomic Energy Agency	TMI three mile island
LOFT loss-of-fluid test	VEGA verification experiments of radionuclides gas/aerosol
LWR light water reactor	VI vertical induction

[☆]*Change History:* December 2019. Markus H.A. Piro, Jean-Christophe Dumas, Brent J. Lewis, William T. Thompson and Fernando C. Iglesias have updated the text and references.

This is an update of Lewis, B.J., Thompson, W.T., Iglesias, F.C., 2012. Chapter 2.20 – Fission Product Chemistry in Oxide Fuels. In: Konings, R.J.M. (Ed.), Comprehensive Nuclear Materials, Elsevier, pp. 515–546.

2.07.1 Introduction

In the present generation of nuclear power reactors, including the light water reactor (LWR) and the heavy water moderated CANDU reactor, the uranium dioxide fuel is used almost exclusively in the form of ceramic pellets that are encased in a zirconium alloy. A mixed oxide (MOX) fuel ($U_{1-\gamma}Pu_{\gamma}O_2$ (where $0 < \gamma < 0.2$ is typical) is also used in LWRs and liquid-metal-cooled fast breeder reactors (FBR; with stainless steel cladding). As the UO_2 and $(U,Pu)O_2$ oxide fuels are irradiated, a large number of fission products are produced. The irradiated oxide fuel forms a multicomponent system consisting of more than 40 main fission product elements as summarized in [Table 1](#).^{1,2} These elements are collected into representative groups that exhibit similar chemical and physical behavior in irradiated fuel (see [Table 2](#)). The fission products may be distributed among several phases, depending on the temperature, pressure, and composition (burnup) of the fuel–element system. The chemical state will also influence the physical properties of the fuel, including the thermal conductivity, swelling, creep, and incipient melting point, as well as the release behavior of the fission products from the fuel matrix because of their relative volatility both under normal operating conditions and during transients.³ Gaseous fission products released to the fuel-to-clad gap and plenum regions (mainly xenon and krypton) may strongly influence the thermal conductance in the fuel-to-clad gap, internal gas pressure, and eventual stresses on the cladding. In addition, the knowledge of the chemical states of the fission products in irradiated fuels and the conditions that cause them is of importance in interpreting the post-irradiation examinations of the discharged fuel, and long-term spent fuel storage and reprocessing.^{4–7}

Table 1 Inventories of the main fission products and actinides in oxide fuel and their expected segregation tendencies

Element	Abundance after 1 year cooling			Segregation tendency ^a	Segregation form ^a
	CANDU (g per t of U) for a burnup of 290 MWh per kilogram of U ^b	Fast neutron fission in oxide fuel (g per t of (U,Pu,f.p.)O ₂) for a burnup of 1% ^c			
		U ²³⁵	Pu ²³⁹		
Se	18			(Like Te?)	(Like Te?)
Br	7			Strong	Uncertain
Kr	101	120	60	Pronounced	Elemental bubbles
Rb	94	130	60	Strong	Oxide (inclusions?)
Sr	246	260	100	Slight	Oxide
Y	126	180	60	None	
Zr	1080	1000	650	Slight	Oxide (inclusions?)
Mo	1140	890	790	Strong	Metallic particles and oxide
Tc	288	220	210	Strong	Metallic particles (and oxide?)
Ru	871	480	800	Strong	Metallic particles (and oxide?)
Rh	235	130	230	Strong	Metallic particles
Pd	511	110	580	Strong	Metallic particles
Ag	42	8	80	Strong	Metallic particles
Cd	32	8	35	Strong	Metallic particles (and oxide?)
Sn	19	32	35	Strong	Metallic particles (and oxide?)
Sb	7	14	14	Strong	Metallic particles
Te	176	140	170	Strong	Metallic or oxide (inclusions?)
I	91	80	100	Strong	Uncertain
Xe	1930	1050	1150	Pronounced	Elemental bubbles
Cs	901	960	950	Strong	Oxide (inclusions?)
Ba	447	390	310	Strong	Oxide (inclusions?)
La	409	290	260	None	
Ce	882	690	630	None	
Pr	378	340	260	None	
Nd	1240	980	870	None	
Pm	78	90	110	None	
Sm	246	140	220	None	
Eu	46	20	40	None	
Gd	35			None	
Np	51			None	
Pu	5250			None	
Am	34			None	

^aBased on extensive studies of LWR and FBR fuel and limited studies on CANDU fuel. Hocking, W.H., Duclos, A.M., Johnson, L.H., 1994. J. Nucl. Mater. 209, 1–26.

^bFor fuel used in the Bruce Nuclear Generating Station. Taken from Hocking, W.H., Duclos, A.M., Johnson, L.H., 1994. J. Nucl. Mater. 209, 1–26.

^cTaken from Kleykamp, H.J., 1985. Nucl. Mater. 131, 221–246.

Table 2 Chemical grouping of fission product elements

Group	Chemical group name	Elements
1	Noble gases	Xe, Kr
2	Halogens	I, Br
3	Alkali metals	Cs, Rb
4	Tellurium group	Te, Se, Sb
5	Alkaline earths	Sr, Ba
6	Noble metals	Ru, Mo, Pd, Rh, Tc
7	Rare earths	La, Nd, Eu, Y, Ce, Pr, Pm, Sm, Zr, Nb

The chemical state of the fuel and fission products can be determined from out-of-pile release experiments, dissolution experiments, post-irradiation and metallographic examination (e.g., γ -scanning, mass spectrometry, and a number of micro-analysis techniques including laser-induced, nuclear, X-ray, secondary ion, and Auger electron),^{1,4,8–13} and thermochemical computations^{14–17} (Section 2.07.3). Thermochemical computations implicitly assume that the system is in thermodynamic equilibrium. However, during and after irradiation, the chemistry of the fuel–fission product system is complicated by several phenomena in which (1) the fission product concentrations increase gradually with irradiation, (2) the chemical properties of the fuel components and of fission products change during and after irradiation due to neutron captures and radioactive decays, (3) the oxygen chemical potential of the fuel changes with fuel burnup and the related production of fission products that can alter the oxygen-to-metal ratio of the fuel, and (4) axial and radial temperature gradients that can affect the distribution of the elements into phases, thereby leading to compositional gradients with material transport by thermal diffusion processes.^{2,5,18,19} There can be substantial migration of some elements, particularly the volatile fission products, which can contribute to a gradient in the oxygen chemical potential within the pellet. Equilibrium calculations can be used only as a basis for the estimation of the chemical state, which requires, as an added complexity, a material transport analysis into the calculation, requiring numerical data for the heat of transport of all elements and some compounds that are not well known.²⁰ Moreover, in the case of failed fuel pins during normal operating conditions, the ingress of water for water-cooled thermal reactors or sodium for FBRs into the element can result in further reactions with the fuel and fission products (Section 2.07.4).^{21,22} The cladding can participate in reactions with the fission products delaying their release into the fuel-to-clad gap or into the coolant system with the possibility of fuel rod failure.²³ Moreover, the corrosive behavior of the fission products in the fuel-to-clad gap can affect fuel performance, possibly leading to fuel failure as a consequence of environmentally assisted stress corrosion cracking (SCC) during power ramping maneuvers.^{24–26} The fission products, fuel, and cladding can also interact among themselves, as well as with the surrounding structural materials, during high-temperature reactor accident conditions, leading to the possibility of fuel dissolution and material relocation (Section 2.07.5).^{13,27–32}

2.07.1.1 General Characteristics of Thermal and Fast Reactor Fuels

In a thermal reactor, such as a Pressurized Water Reactor (PWR), the high-pressure coolant (~ 15.5 MPa) enters the assembly structure at a temperature of $\sim 280^\circ\text{C}$ and exits at $\sim 325^\circ\text{C}$, yielding a maximum external cladding temperature of approximately 350°C .³³ These coolant conditions can lead to significant corrosion at the external surface of the cladding. PWR oxide fuels typically operate at an average linear power rating of $13\text{--}19\text{ kW m}^{-1}$ and with peak powers up to 40 kW m^{-1} .³⁴ For these cladding temperatures and fuel ratings, the fuel has a centerline temperature of around $1200\text{--}1300^\circ\text{C}$, which leads only to small fuel restructuring and relatively low fission gas release.³³ The fuel will reside in the reactor for three or more cycles, for a given cycle of 12–18 months (the refueling scheme that is used varies depending on the operator. For example, some utilities prefer 12 mo cycles, while others prefer 18 mo cycles), reaching a fuel burnup of $\sim 35\text{--}55\text{ GWd tU}^{-1}$. In contrast, CANDU fuel operates at much higher fuel ratings of up to 63 kW m^{-1} but for considerably shorter fuel burnups of 7.5 GWd tU^{-1} to limit the internal fission gas pressure below that of the coolant pressure so that clad liftoff does not occur for the collapsible sheathing design. The fuel centerline temperature in CANDU fuel can therefore reach temperatures over 2000°C under normal operating conditions.

In the SUPERPHENIX FBR, the fuel had a much higher power flux than conventional PWRs of $\sim 46\text{--}53\text{ kW m}^{-1}$.^{33,35} The liquid sodium coolant is at a lower hydrostatic pressure of ~ 0.2 MPa with a much higher temperature of 400°C at the bottom of the pin cluster and can reach over 600°C at the exit of the maximum-rated assembly. The neutrons have a higher energy spectrum with a total neutron flux that can reach $6 \times 10^{15}\text{ n cm}^{-2}\text{ s}^{-1}$. For these higher coolant temperatures and linear power ratings, the fuel centerline temperature can reach in excess of 2000°C under normal conditions, which can result in relatively large fuel restructuring and large fission gas release rates.

2.07.1.1.1 Plutonium distribution

²³⁹Pu is produced from the capture of epithermal neutrons in the resonances of ²³⁸U with subsequent β -decay. Other Pu isotopes are also formed, but their contribution to the overall fission yield is small. Fig. 1 presents measurements of Pu across a pellet cross-section for a thermal reactor pin. It is seen that Pu is uniformly distributed in the interior of the fuel, whereas its concentration increases steeply at the fuel surface because of enhanced neutron capture in this region. The high surface concentration affects the

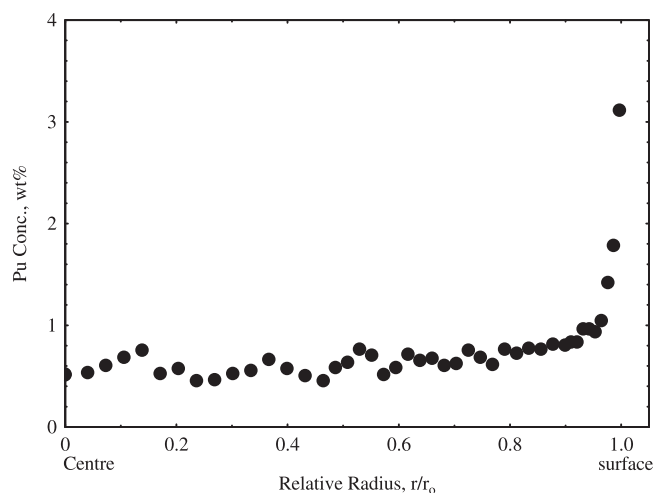


Fig. 1 Diametral concentration profile of Pu across a fuel rod. Copied from Walker, C.T., Bremier, S., Portier, S., Hasnaoui, R., Goll, W., 2009. J. Nucl. Mater. 393, 212–223.

radial power generation in the fuel rod. This result is of particular importance for natural-uranium fueled reactors. This so-called “rim effect” should be taken into account for a proper analysis of the radial temperature distribution in fuel rods. Furthermore, the rim effect has a significant effect on the local chemistry of the fuel, most notably the local oxygen chemical potential.³⁶

2.07.1.1.2 Radial dependence of fuel stoichiometry after irradiation

The oxygen potential of fuel during irradiation can be estimated from the oxidation states of the fission products, cladding, and clad impurities (see Sections 2.07.1.2 and 2.07.3). It is estimated from calculations up to 5 at% burnup that there is an increase in the O/M ratio of about 0.0013 per at% burnup.¹⁹ However, measurement of oxygen diffusion into the zirconium cladding (see Fig. 2) shows that such excess oxygen can diffuse into the zirconium cladding, resulting in a fuel stoichiometry with an O/M ratio very close to 2.00 and the formation of zirconia on the inner side.¹⁹ In addition, changes in UO₂ pellet stoichiometry during storage in air, that is, prior to fuel rod fabrication for periods of up to 32 years, show no increase in the stoichiometric deviation.³⁷

2.07.1.2 Fission Product Classifications in Irradiated Fuels

The intrinsic mobility of fission products will depend on the charge state of the atomic species that migrate by solid-state diffusion through the lattice of the fuel. When fission product atoms reach a free surface, they may form thermodynamically favored compounds. The chemical form will determine the subsequent gas-phase mass transport (i.e., vaporization). The release of fission products is also determined by the solubility of the fission products in the UO₂ lattice. During irradiation, the noble gases are distributed dynamically between a fission-induced solution within the oxide lattice and their nucleation and precipitation into intragranular and intergranular bubbles. The chemical state of the fission products can therefore be classified into the following main groups on the basis of numerous elemental analyses of irradiated LWR and FBR fuels (see Table 1 and Fig. 3)^{2,5}:

- (1) fission gases and other volatile fission products: Kr, Xe, Br, and I;
- (2) fission products forming metallic precipitates: Mo, Tc, Ru, Rh, Pd, Ag, Cd, In, Sn, Sb, and Te;
- (3) fission products forming oxide precipitates: Rb, Cs, Ba, Zr, Nb, Mo, and Te;
- (4) fission products dissolved in the fuel matrix: Sr, Zr, Nb, and the rare earths Y, La, Ce, Pr, Nd, Pm, and Sm.

There are continuous transitions between the four groups as the critical concentration conditions for new phase development are surpassed because of increased burnup. Fig. 4 illustrates the evolution of the fission and activation product inventory in PWR fuel with respect to burnup. It is important to note that not only are the absolute proportions of fission products accumulating with time, but the relative proportions of fission products are also changing with respect to one another. For example, the plutonium concentration increases quite rapidly up until around 20 GWd/t(U), which is mainly due to the production of ²³⁹Pu via neutron activation of ²³⁸U. After that point, the rate of activation of ²³⁹Pu is comparable to its rate of depletion, which is why the Pu content does not rapidly increase at higher burnups. On the contrary, some fission product elements like Xe, Mo, and Zr continue to increase in concentration throughout the entire irradiation.

Since the process of fission, by its nature, contributes to an increase in the total number of moles of elements of metal, M, in relation to the virtually fixed number of moles of oxygen, O, the O/M ratio of the fuel slowly increases during burnup. Since the fuel is not homogenous and secondary phases form on the grain boundaries during the course of irradiation, the total O/M ratio of the fuel differs from the O/M ratio in the fluorite phase. The different fission product elements have widely varying ability to chemically associate with oxygen. This matter is captured in the diagram in Fig. 5 attributed to Ellingham, originally developed in

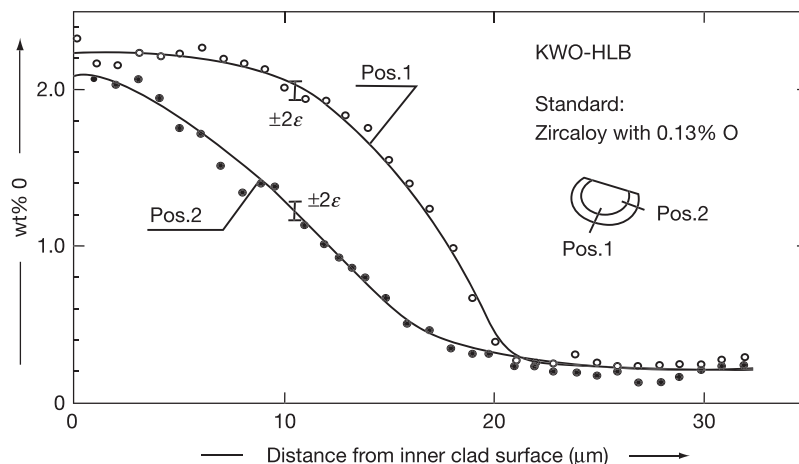


Fig. 2 Oxygen concentration in function of distance from the sheath inner surface. Modified from Kleykamp, H., 1979. J. Nucl. Mater. 84, 109–117.

A		T										B					
I A	II A											III B	IV B	V B	VI B	VII B	
Li	Be											B	C	N	O	F	Ne
Na	Mg	III A	IV A	V A	VI A	VII A		VIII		I B	II B	Al	Si	P	S	Cl	Ar
K	Ca	Sc	Ti	V	Cr	Mn	Fe	Co	Ni	Cu	Zn	Ga	Ge	As	Se	Br	Kr
Rb	Sr	Y	Zr	Nb	Mo	Tc	Ru	Rh	Pd	Ag	Cd	In	Sn	Sb	Te	I	Xe
Cs	Ba	La	Hf	Ta	W	Re	Os	Ir	Pt	Au	Hg	Tl	Pb	Bi	Po	At	Rn
Fr	Ra	Ac															
		Ce	Pr	Nd	Pm	Sm	Eu	Gd	Tb	Dy	Ho	Er	Tm	Yb	Lu		
		Th	Pa	U	Np	Pu	Am	Cm	Bk	Cf	Es	Fm	Md	No	Lr		

	Volatile fission product		Metallic precipitates (alloys)		Ceramic precipitates (oxides)		Oxides dissolved in the fuel
--	--------------------------	--	--------------------------------	--	-------------------------------	--	------------------------------

Fig. 3 The chemical state of the fission products in oxide fuels. Adapted from Kleykamp, H., 1985. J. Nucl. Mater. 131, 221–246.

support of understanding metallurgical processing practices. The diagram gives the standard Gibbs energy of isothermal formation of oxides from pure metal (or element) and oxygen gas at one atmosphere pressure as a function of temperature. To permit easy comparison of the relative affinity for oxygen, all oxide formation reactions on the diagram are based on one mole of O_2 instead of the more usual convention of one mole of oxide. In this way, recognition is given to the different number of moles of oxygen in the formula mass when comparing, for example, the relative ability of a comparable quantity of O_2 to react with U (1 mol) or La ($4/3$ mol) to form UO_2 (1 mol) or La_2O_3 ($2/3$ mol). The lowest lines on the Ellingham diagram are thus associated with the elements (rare earths or lanthanides, Ln) that form the most stable of oxides. By comparison, elements associated with lines near the top of the diagram, such as Pd, are not strongly reactive with oxygen and may, when heated to temperatures that pass through the top of the diagram ($\Delta G \geq 0$), not combine with oxygen at all.

The reaction of metal with oxygen is sensitive to the concentration or partial pressure of oxygen. The equilibrium oxygen pressure for the reaction involving a typical fission product may be written as³⁸



where (FP) and (FP) O_n denote the fission product element and its oxide, respectively. The valence of the fission-product cation in the oxide form is $2n$. The equilibrium constant for the above equation yields the oxygen partial pressure:

$$p_{O_2} = \exp\left(\frac{\Delta G_p}{RT}\right) \quad (2)$$

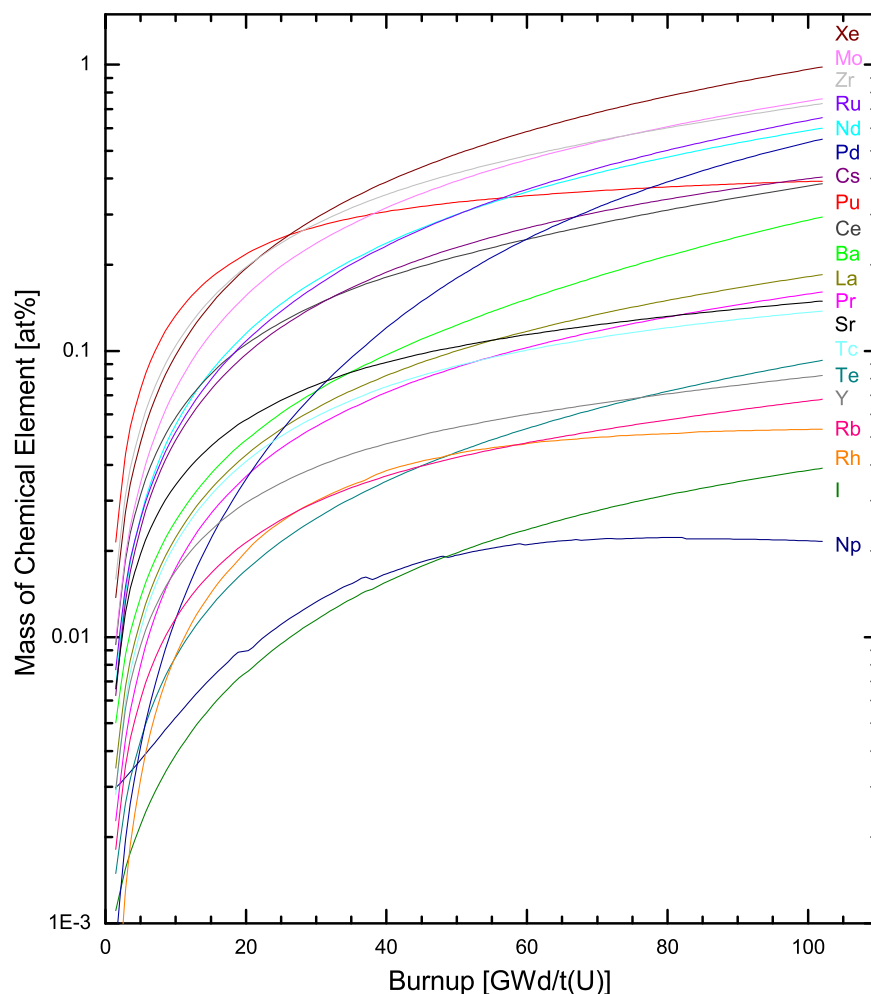


Fig. 4 The calculated fission product inventory in PWR evolves with respect to burnup. Reproduced from Piro, M.H.A., Banfield, J., Clarno, K.T., *et al.*, 2013. Coupled thermochemical, isotopic evolution and heat transfer simulations in highly irradiated UO_2 nuclear fuel. *J. Nucl. Mater.* 441, 240–251.

where R is the ideal gas constant and ΔG_p is the standard Gibbs energy of formation of the fission-product oxide per mole of oxygen at 1 atm pressure at temperature T . At 1500K, PdO has a standard Gibbs energy of formation of $+50 \text{ kJ mol}^{-1}$ of O_2 , and yields a $p\text{O}_2$ (where pure oxide and pure metal can coexist) of 50 atm, whereas for La_2O_3 with a standard Gibbs energy of formation of -960 kJ mol^{-1} of O_2 , the equilibrium $p\text{O}_2$ is $\sim 10^{-35}$ atm. The equilibrium partial pressure of oxygen therefore provides an equivalent means to discuss relative oxide stabilities. From Eq. (2), it is apparent that ΔG_p and $RT \ln p\text{O}_2$ are equivalent, and the latter is sometimes called the (relative) oxygen (chemical) potential.

With burnup, the liberated oxygen will associate with U, Pu, and La but may not be in sufficient supply to combine with Pd and other less oxidizing elements, which are located near the top of the Ellingham diagram. In terms of oxygen potential, if the Gibbs energy of formation of the given fission product lies below the fuel oxygen potential, as shown in Fig. 5, the element will be capable of associating with oxygen in the fuel matrix and an oxide of that fission product can be said to form; if the fission product point is above the chemical potential in the fuel, the fission product will exist as an element in the fuel (in a separate metallic phase). Thus, Pd is expected to be found as a metal and La as an oxide, as depicted in Fig. 3. In the case of molybdenum, the Gibbs energy of formation of MoO_2 is very close to the lowest value of the oxygen potential that can be expected in irradiated fuel and the fission product may be present as an oxide dissolved to some small extent in the fuel matrix (as MoO_2) or as an element in a metallic inclusion phase with Pd and other elements (Tc, Ru, Rh).³⁹ Under certain conditions of high oxygen potential not normally encountered, a mixed oxide phase with uranium may also appear, that is, UMoO_6 . Molybdenum therefore provides an important buffering capability on the oxygen potential in oxide fuel,² or equivalently, a means of inferring what the oxygen potential may have been in post-irradiation examination of irradiated fuel. A summary of the chemical destiny of fission products is given in Table 3.

The fission-product oxides can dissolve in the fluorite structure of the fuel matrix by replacing a uranium or plutonium cation on the normal lattice site. When a $4+$ valence fission product (e.g., Zr^{4+}) enters the lattice, there is no change in the electrical

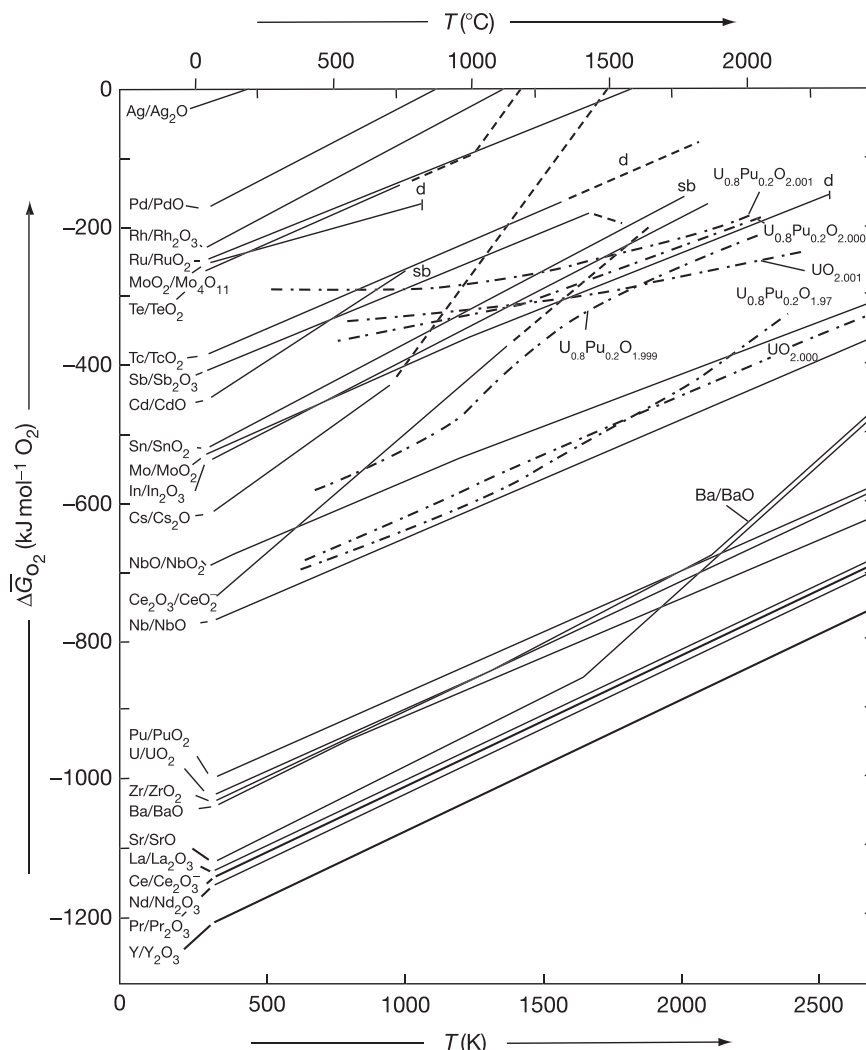


Fig. 5 Relative partial molar Gibbs energies of oxygen of the fission product oxides and of UO_{2+x} and $\text{U}_{0.8}\text{Pu}_{0.2}\text{O}_{2\pm x}$; d: oxide decomposes; sb: oxide sublimes. Modified from Kleykamp, H., 1985. J. Nucl. Mater. 131, 221–246.

neutrality of the crystal – the Zr^{4+} replaces a position otherwise occupied by U^{4+} . However, if the charge of the fission-product cation is lower than the host U^{4+} ion (as with a rare earth or lanthanide oxide of the form M_2O_3 with a charge of $3+$), the site occupancy of the lattice is altered to achieve electrical neutrality. In this case, oxygen anion vacancies are created. On the other hand, under sufficiently oxidizing conditions, some $4+$ uranium ions may oxidize to $5+$ or $6+$, giving rise to vacancies in the cation lattice. Elements that readily substitute in size for uranium in the fluorite structure, such as the actinides and rare earths, are expected to remain atomistically dispersed within the host matrix.²

The alkaline earth cations Ba^{2+} and Sr^{2+} have large ionic radii and therefore form a separate oxide phase generally in combination with other elements. Sr is partially soluble in the UO_2 lattice, whereas Ba does not dissolve in the fuel matrix. In the local presence of sufficient zirconium, the stable forms of the oxides are the zirconates, BaZrO_3 and SrZrO_3 . Fission products that have limited solubility in UO_2 will segregate to the grain boundaries and eventually to the void space within the element (Table 1). Up to several percent of the noble gas inventory of xenon and krypton can typically be found in the fuel-to-clad gap, depending on the fuel irradiation history. These volatile species can be segregated into numerous microscopic bubbles.^{12,40}

The so-called “white inclusions” are detected in post-irradiation studies of UO_2 and $(\text{U}, \text{Pu})\text{O}_2$ fuels. These metallic precipitates, which are composed of Mo, Tc, Rh, Ru, and Pd, form a quinary alloy that crystallizes (given the proportions involved) in most cases in a close packed hexagonal structure. In addition, a “gray oxide phase” perovskite structure containing different combinations of Ba, Cs, Zr, Mo, U, and possibly other elements (rare earths or lanthanides Ln), for example, with a composition of $\text{Ba}(\text{U}, \text{Pu}, \text{Zr}, \text{Ln}, \text{Mo})\text{O}_3$, has also been observed for higher power/burnup LWR and FBR fuels.² The same fission products as well as less abundant ones (Te, Sr, I, Sn, Sb) have also been detected in deposits formed on the fuel cladding and/or within a central void under extreme conditions.^{2,8,11,14}

Table 3 Probable chemical and physical states of fission products in mixed-oxide fuels^a

Chemical group	Physical state	Probable valence
Zr and Nb	Oxide in fuel matrix; some Zr in alkaline earth oxide phase	4 +
Rare earths	Oxide in fuel matrix	3 +
Ba and Sr	Alkaline earth oxide phase	2 +
Mo	Oxide in fuel matrix or element in metallic inclusion	4 + or 0
Ru, Tc, Rh, and Pd	Elements in metallic inclusion	0 +
Cs and Rb	Elemental vapor or separate oxide phase in cool regions of fuel	1 + or 0
I and Te	Elemental vapor; I may be combined with Cs and CsI	0 or 1 –
Xe and Kr	Elemental gas	0

^aFor near stoichiometric fuels. Reproduced from Olander, D.R., 1976. Fundamental Aspects of Nuclear Reactor Fuel Elements. TID-26711-P1. Technical Information Center. US Department of Energy.

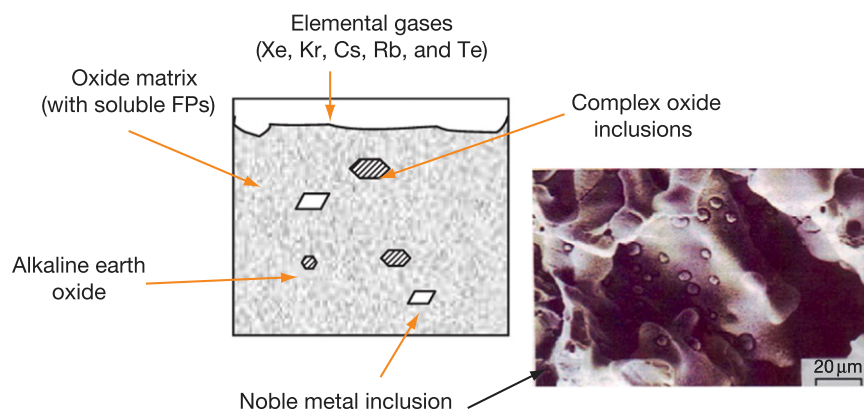


Fig. 6 Schematic of irradiated fuel. The photograph shows a secondary electron image of the metallic Mo-Tc-Ru-Rh-Pd precipitates on the surface of the central void of a fast breeder reactor mixed-oxide pin at a local burnup of 6.4%. Adapted from Olander, D.R., 1976. Fundamental Aspects of Nuclear Reactor Fuel Elements. TID-26711-P1. Technical Information Center, US Department of Energy.

Although the conventional Ellingham diagram in Fig. 5 provides a quite useful means to assess whether the fission product exists as an oxide or metal for the given oxygen potential, this approach does not take into consideration the possibility of more complex oxide fission product phases (e.g., BaZrO_3 and Cs_2MoO_4). Another computationally intensive methodology, that of Gibbs energy minimization, is required. This technique provides a means to determine the chemical speciation of the fission products and their effect on the fuel oxygen potential with burnup. This computation is complicated by a continually changing fission product concentration, diffusion, and oxygen potential with irradiation and decay, as well as by very steep temperature gradients within the fuel (see Section 2.07.1). However, this type of analysis can account for (1) the O-U system (including nonstoichiometry); (2) soluble fission products; (3) noble metals (Mo, Rh, Pd, Ru, and Tc); (4) zirconate, uranate, and molybdate phases; (5) second metal solid solution $\text{U}(\text{Pd-Rh-Ru})_3$; and (6) volatile species within the inert gas phase (see Fig. 6).

2.07.2 Chemical State of Fission Products in Irradiated Oxide Fuels

It is difficult to perform direct measurements on irradiated fuel samples to ascertain the chemical state of the fission products. A combination of multiple indirect methods is therefore more commonly used, including an observation of measured deposition patterns or phase changes, as well as experiments performed in hot-cells under strict environmental control in the handling of irradiated materials. Nevertheless, the chemical state of some particular elements remains elusive and thermodynamic analysis becomes an important tool for such assessments. A description of the more common experimental techniques employed, and major observations from these investigations, are provided in great detail by Manara *et al.*⁴¹

In-pile measurements are difficult to interpret because of the many chemical reactions that can occur with the release of fission products. For such interpretation, other supporting tests are performed in hot-cells or in the laboratory with irradiated or unirradiated fuel specimens. Under these experimental conditions, there is better control, where more complex and accurate measurement equipment can be used.

As mentioned, the initial UO_2 or $(\text{U, Pu})\text{O}_2$ fuel will change during irradiation to a multicomponent multiphase system with the production of fission products. In general, as mentioned earlier, irradiated fuel displays five identifiable phases: (1) fuel-fission product oxide solid solutions, (2) perovskite oxides known as the “gray phase,” (3) metallic inclusions, (4) phases rich in Pd and

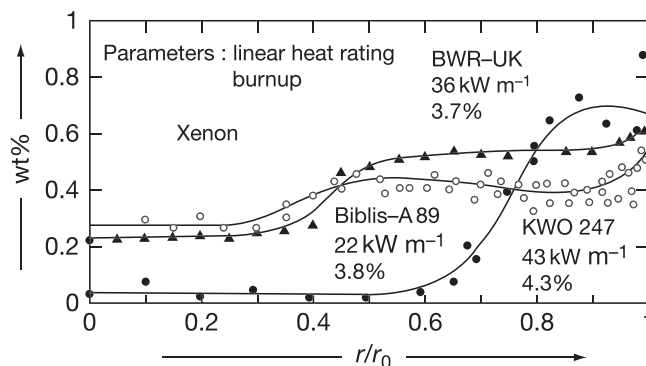


Fig. 7 Xe concentration (as measured by electron microprobe) as a function of the relative pellet radius in pressurized water reactor. Modified from Kleykamp, H., 1985. *J. Nucl. Mater.* 131, 221–246.

Te, and (5) metallic actinide-noble metal compounds at low oxygen partial pressures.² This section describes the major behavior characteristics of fission products, fissionable material, and possible fission product reactions with the clad.

2.07.2.1 Volatile Fission Products

Since noble or inert gases are by nature not chemically reactive, the Kr and Xe isotopes can be easily measured by γ -spectroscopy methods, depending on their half-life. Medium- and long-lived isotopes can be determined from in-pile experiments with correction for decay due to transport to the detector station. In-cell tests allow of a direct γ -measurement, with relatively low background, thereby permitting observations of the shorter-lived isotopes. In-reactor experiments, in which the gap inventories are swept away from the fuel to γ -detectors, have been performed to obtain information on short-lived fission product release behavior of volatile isotopes either directly or by measuring their decay daughters in the gas flow or on charcoal cold traps.

Noble gases are mainly released from the UO_2 matrix by diffusion from the fuel grains to the grain surfaces where they precipitate into grain boundaries bubbles. Tunnels form on grain edges after bubble interconnection, resulting in a release into the fuel-to-clad gap. Some of these tunnels are observed in ceramographs at room temperature. Very small amounts of noble gas isotopes can also be directly released from the pellet surfaces into the gap by recoil and knock-out processes, or produced by the decay of bromine and iodine isotopes that are already in the gap region or have deposited on pellet and clad surfaces. **Fig. 7** shows the Xe concentration (wt%) distribution for three fuel rods irradiated to burnups between 3.7 and 4.3 at% at linear powers of 22, 36, and 43 kW m^{-1} as measured by electron microprobe.

Xe release occurs at the central region of the pellet where the highest temperatures were achieved during irradiation.^{19,42} In hot-cell experiments, where irradiated fuel specimens were subjected to temperature ramps, an initial burst of noble gas is observed followed by a significantly lower release rate. This burst arises from a release of noble gases from the grain boundaries, whereas the slower release occurs from diffusion within the fuel grains.^{43,44} The fractional release from the fuel depends on the stoichiometry of the UO_2 where higher releases occur at higher stoichiometric deviations.⁹ Note that **Fig. 7** represents the Xe concentration in the fuel, which is not directly indicative of the local release – most of the gas remains in bubbles.⁴⁵

The Xe concentration distribution in a single UO_2 grain has been reported.⁴⁶ This distribution is consistent with a diffusional release process. Measurements at the Harwell Laboratory have shown that the gas release depends on the heating rate with a maximum release resulting between 10 and 20 K s^{-1} . This observation suggests that the migration of fission gases is a complicated process, involving an interaction between the gas atoms and bubbles within the UO_2 grains and on the grain boundary surfaces.^{44,47}

Volatile fission products shown in **Fig. 3** are released from the fuel matrix similar to that of the noble gases. In addition, Cs isotopes can be considered as part of this group if the fuel temperatures are higher than 1600K. In particular, migration of cesium from the fuel to the pellet surface is consistently reported on axial γ -scans (with high concentrations at the pellet-to-pellet interfaces). In some in-pile and in-cell experiments, the fractional release of these volatile isotopes is very difficult to distinguish from the fractional releases of the noble gases. Other studies, however, suggest that Te and I may be released significantly faster than that of the noble gases.^{48–50}

The presence of some compounds (i.e., CsI) in the gap is well supported by experimental evidence.^{13,19} What is not clear is whether the CsI has already formed before reaching the gap or if it is formed in the gap at low burnups (< 0.5 at%).^{9,27} In FBR, the presence of Mo and Cs compounds was determined in the fuel-to-clad region with electron microprobe Wavelength-dispersive X-ray spectroscopy.⁵¹ Also, the iodine volatility can be significantly affected by the oxidation state of Mo.³⁰

Volatile fission products in the gap can react among themselves, resulting in a changing chemical speciation. At normal operation temperatures, the reaction kinetics for formation and radiolytic decomposition may dominate the abundance of some chemical species.¹³ In the case of Cs, I, and Zr (see Section 2.07.2.3), the kinetics of formation/decomposition of CsI and Zr iodides are possible factors in the mechanism of SCC. Other compounds are also expected to be present in the gap as suggested from thermodynamic calculations; however, the confirmation of their existence requires further experimentation.

2.07.2.2 Distribution and Segregation of Fission Products

Fission products can be segregated because of their migration to specific locations (e.g., intragranular segregations, grain boundaries or pellet surfaces). The neutron flux inside a pellet decreases from the surface to the center (self-shielding) and the fission events in the pellets follow this distribution. In particular, the fission events per unit volume are the highest at the pellet surface. In this region, the fission of ^{239}Pu provides an additional contribution of fission products (see Section 2.07.1.1.1). The noble gases will segregate into bubbles that populate the grain boundaries, which is complicated in the high burnup structure due to the subdivision of the original grains.

Metallic inclusions are commonly observed in ceramographs from irradiated samples. They are formed by isotopes of Mo, Tc, Ru, Rh, Pd, Ag, Cd, In, Sn, Sb, and Te.^{3,10} These inclusions are found at the surface of the grain boundaries and are associated, in general, with grain boundary and intragranular bubbles. Under certain conditions, these precipitates inhibit the movement of the grain boundary bubbles (i.e., bubble pinning). A thermodynamic-based estimation of some possible compounds is detailed in Section 2.07.3.2.2.

Despite the low releases associated with these inclusions, under certain environmental conditions (e.g., highly oxidizing or reducing), some of the components of these precipitates can be oxidized or reduced forming other compounds of higher volatility that can be released from the fuel matrix. Examples of this behavior are for the cases of Ru and Ba. Under reducing conditions, the Ru release is very limited; however, Ru release is much faster in steam and even more so in air (probably as RuO_4 and/or RuO_3).^{52,53} Nb behavior is similar to Ru.³¹ Ba exhibits a different behavior, in which very small quantities of Ba are released in oxidizing conditions (steam or air) probably because of the low volatility of the oxide. On the other hand, significant releases of Ba were measured under reducing conditions.³¹

In addition, Cs, Ru, Te, and Ba have been consistently found at the cracks in the pellet and on the clad inner surface. A surface enrichment of these fission products is common, whereas Cd, Mo, Sr, and I have been occasionally detected.¹ Despite the fact that the total extent of segregation appears to depend on the irradiation history, the relative abundance of individual segregates show significant variation. This variability could be attributed to the slight differences in initial fuel stoichiometry, which can have a major effect on the chemistry of some elements (Te, Mo, Cd) as well on thermal diffusion rates.¹ Furthermore, a widespread distribution of segregated fission products, in particular Cs, was observed along the length of the inner surface of the clad.⁸ Even more diverse element segregation was observed at the ends of the fuel rods where high levels of Ba, Sr, Te, I, and Cd were found relative to that of Cs. These findings are consistent with the premise that the fission products migrate in the hotter central region of the pellet and then radially toward the clad at the pellet-to-pellet interfaces.⁵⁴ In mixed oxides containing considerable Si impurities, agglomeration of these elements without fuel constituents were deposited at the fuel crack openings.⁵⁵

2.07.2.3 Reaction of Fission Products With Zirconium Alloy Cladding

Fission fragments will deposit on the inner surface of the cladding.⁵⁴ Some of these species can diffuse into the clad, while others can attack the clad thereby initiating cracks that can later progress with the formation of through-wall cracks. Oxygen will diffuse into the cladding and contribute to its oxidation state. Measurements have shown deposits of Sr, Cs, Pu, and Am.⁵⁶

The corrosion behavior of zirconium by Te was reported with a duplex corrosion layer consisting of zirconium telluride and zirconium oxide for an oxygen potential less than -500 kJ mol^{-1} . Zirconium telluride is absent for oxygen potentials over -430 kJ mol^{-1} .²³ Te can diffuse into the clad and after the segregation of the Sn during Zircaloy oxidation, can combine to form tin telluride (see Section 2.07.5).²⁸

The chemical reaction between some corrosive fission product(s) and the cladding can lead to Pellet Cladding Interaction (PCI), which is a mechanism involving SCC. In this mechanism, fission products such as Cs, Cd, or I can attack the clad inducing crack initiation, which then progress through the cladding by intragranular and transgranular cracking modes. Fractographic studies indicate that the most probable species responsible for this crack formation is iodine.³⁴ Zr atoms can be removed from the crack tip by the formation of several zirconium iodides.³⁴ It has been suggested that the necessary reactive iodine in the gap can be produced by radiolysis of CsI, which is generally quite stable, due to fission fragment recoil and knockout from the fuel surface.²⁴

2.07.2.4 Oxygen in Zirconium Alloy cladding

The oxidation of zirconium in steam was recognized early as an important source of heat during postulated accidents. Parabolic rate correlations have been developed from isothermal oxidation tests. Also, more sophisticated theoretical models, based on the assumption that oxygen diffusion is the controlling mechanism for this phenomenon, have been developed.⁵⁷ During the oxidation process, the Sn in the oxide phase is precipitated in a series of concentration beads in a plane parallel to the oxide surface. This observation indicates that precipitation occurs at a particular oxygen concentration in the oxide phase.

The heat of the oxidation reaction in steam is -616 kJ mol^{-1} at 298K and in air $-1100 \text{ kJ mol}^{-1}$ at 298K.⁵⁸ This difference is reconciled by the amount of energy required to decompose the H_2O molecules. Recently, isothermal experiments performed in air have shown that oxidation rates in the temperature range between 700 and 1500K are considerably faster than for steam at the same temperature.⁵⁸ More experimental work is required, however, to understand the kinetic behavior during temperature transients and the effect of steam pre-oxidation.

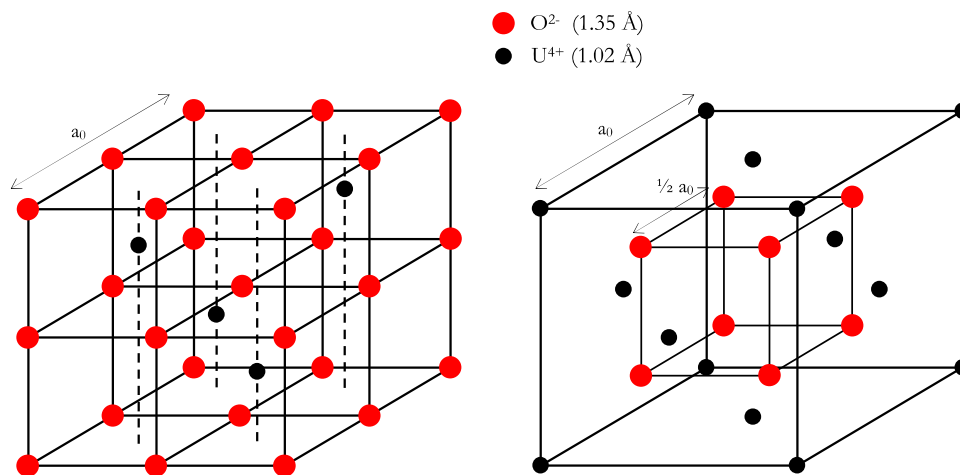


Fig. 8 The uranium dioxide (UO_2) fluorite crystal structure is shown identifying the Simple Cubic (SC) anion sublattice (left) and the Face Centered Cubic (FCC) cation sublattice (right). Reproduced from Piro, M.H.A., 2011. *Computation of Thermodynamic Equilibria Pertinent to Nuclear Materials in Multi-Physics Codes*. PhD Thesis. Kingston: Royal Military College of Canada.

2.07.3 Thermodynamic Modeling of Oxide Fuels

When many elements are involved in possible reactions, particularly when more than one phase may arise, the broad thermodynamic judgments made using an Ellingham diagram are inadequate and may even lead to false conclusions in view of the simplifying assumptions that must necessarily be made. This is because the Ellingham diagram, which is an effective tool at evaluating favorable oxidation reactions, is limited to specific reactions and cannot capture multi-component multi-phase systems. A more general and computationally intensive methodology is required – namely, Gibbs energy minimization.

Gibbs energy minimization, which retains the cornerstone principles of the Ellingham diagram, involves the systematic redistribution of elements among the many possible species and phases in such a way as to preserve the number of moles of each element in a closed system. The fundamental premise of the technique is to determine a unique combination of species and phases that yields a global minimum in the Gibbs energy function of a closed isothermal-isobaric system subject to appropriate constraints. Finding a global minimum in the Gibbs energy of a system is equivalent to respecting the first and second laws of thermodynamics: energy is conserved and entropy of the universe tends to a maximum. This process is described in further detail by Piro.⁵⁹

2.07.3.1 Uranium–Oxygen Binary System

A thermodynamic treatment of the complete U–O system with particular emphasis on the location of the UO_{2+x} – U_4O_9 phase boundary and the behavior of $p\text{O}_2$ over the entire range of UO_{2+x} can be developed.^{22,60} Stoichiometric UO_2 adopts the fluorite crystal structure, which is shown in Fig. 8, and takes on the $[Fm\bar{3}m]$ Hermann-Mauguin space group. The perfect crystal structure is shown in Fig. 8, whereby the oxygen anions (O^{2-}) are shown in red and are on a simple cubic lattice and uranium cations (U^{4+}) are shown in black on an FCC lattice.

Non-stoichiometric uranium dioxide consists of both Type 1 and Type 2 interstitial sites, in addition to vacancies. The various oxidation states of uranium (i.e., $2+$, $3+$, $4+$, $5+$, and $6+$) ensures compliance to charge neutrality. Fig. 9 illustrates a more realistic crystal structure of urania with these point defects and how a departure from stoichiometry can be accommodated.

There are various approaches to the modeling of the UO_{2+x} . One approach taken by the RMC Fuel Thermochemical Treatment¹⁵ is to approximate this phase as a mechanical mixture of the following species: UO , UO_2 , and UO_3 . This has been represented by a regular substitutional model with interaction parameters to capture non-ideal behavior and Kohler-Toop interpolation of binary sub-systems. Another approach by Guéneau *et al.*⁶¹ represents UO_{2+x} by the compound energy formalism with three sublattices. In this model, the first sublattice represents uranium cations, the second sublattice represents oxygen anions on their normal lattice sites with vacancies, and the third sublattice represents oxygen anions and vacancies on interstitial sites.

The mixing process of constituents involves the distribution of cations of uranium and anions of oxygen over the allowed positions in this structure. The non-stoichiometry arises because not all the uranium cations have the same charge. On the premise that only U^{4+} ions and U^{5+} ions exist, the conceptual mixing process involves a distribution of U^{4+} and U^{5+} cations within a regular arrangement of O^{2-} anions. However, a certain fraction of the cationic lattice sites must be vacant to respect charge neutrality constraints. This vacancy fraction is related to the value of x in UO_{2+x} .

The actual Gibbs energy recognizes deviations from random distribution in the actual entropy of mixing as well as the heat effects when the conceptual dissolution of the component oxides occurs. The departure term, or excess Gibbs energy of mixing, is essentially an adjustment expression to experimental data involving, typically, a short series in the concentration variable with

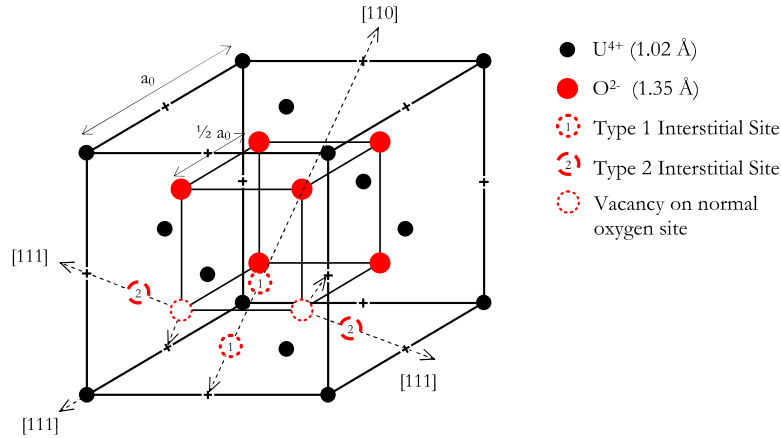


Fig. 9 Defect complex of UO_2 highlighting Type 1 and Type 2 interstitial sites from Fig. 8. Reproduced from Piro, M.H.A., 2011. Computation of Thermodynamic Equilibria Pertinent to Nuclear Materials in Multi-Physics Codes. PhD Thesis. Kingston: Royal Military College of Canada.

temperature-dependent coefficients. A model of UO_{2+x} together with Gibbs energy expressions of other stable species and phases in the U-O system can collectively be used to construct a phase diagram of the system.

Isobaric lines of gaseous O_2 and UO_3 partial pressure can be added to the phase diagram, as shown in Fig. 10. Since the partial oxygen pressure in the UO_{2+x} field is very low, it is more useful to express this partial pressure as the equivalent $\text{H}_2/\text{H}_2\text{O}$ proportion

(see Fig. 11), using the temperature dependent equilibrium constant for the process:



An expression can therefore be derived relating the hydrogen-to-steam partial pressure ratio for the LWR system, temperature T (in K), and the equilibrium stoichiometric deviation x_e ²²:

$$\begin{aligned} \log\left(\frac{p_{\text{H}_2}}{p_{\text{H}_2\text{O}}}\right) = & 5706.8 + 0.1245T - 5.482 \\ & \times 10^{-6}T^2 + \frac{4,296,016}{T} - 1550.95 \log(T) \\ & - \frac{1,772,730 \log(T)}{T} - \frac{155,930,360}{T^2} \\ & + \log\left(\frac{1-x_e}{x_e}\right) - 0.9158x_e - 16.08x_e^2 \\ & + 75.15x_e^3 - 251.51x_e^4 \end{aligned} \quad (4)$$

Eq. (4) is in excellent agreement with the thermodynamic treatments of Lindemer-Besmann⁶² and Blackburn.⁶³ Similarly, for the CANDU system, using the properties for heavy water, the $(\text{D}_2/\text{D}_2\text{O})$ variation of the UO_{2+x} non-stoichiometry is²²

$$\begin{aligned} \log\left(\frac{p_{\text{D}_2}}{p_{\text{D}_2\text{O}}}\right) = & \log\left(\frac{p_{\text{H}_2}}{p_{\text{H}_2\text{O}}}\right) + 1.76985 \\ & - \frac{333.783}{T} - 0.488145 \log(T) \end{aligned} \quad (5)$$

These expressions are shown as they relate to the U-O phase diagram in Fig. 11 and indicate that there is little difference for the prediction of the atmospheric oxygen potential between light and heavy water. It is noteworthy that the constant ratio lines converge about the 2:1 ratio for the O:U proportion at temperatures below about 500°C. This implies that contact of steam with UO_2 below 500°C imparts very little disturbance to the UO_2 stoichiometry; higher temperatures are required to create a significantly hyperstoichiometric UO_2 . Eqs. (4) or (5) can be used, for example, to estimate fuel hyperstoichiometry arising from the penetration of steam/heavy water vapor through the cracks in the fuel pellets of defective elements (Section 2.07.4).²²

2.07.3.2 Phase Diagram Studies of Fission Products in Oxide Fuels

Thermodynamic models can be developed using Gibbs energy minimization to account for the influence of the fission products on the fuel oxygen potential with burnup.⁶⁴ The development of a complete thermodynamic model and thermochemical database

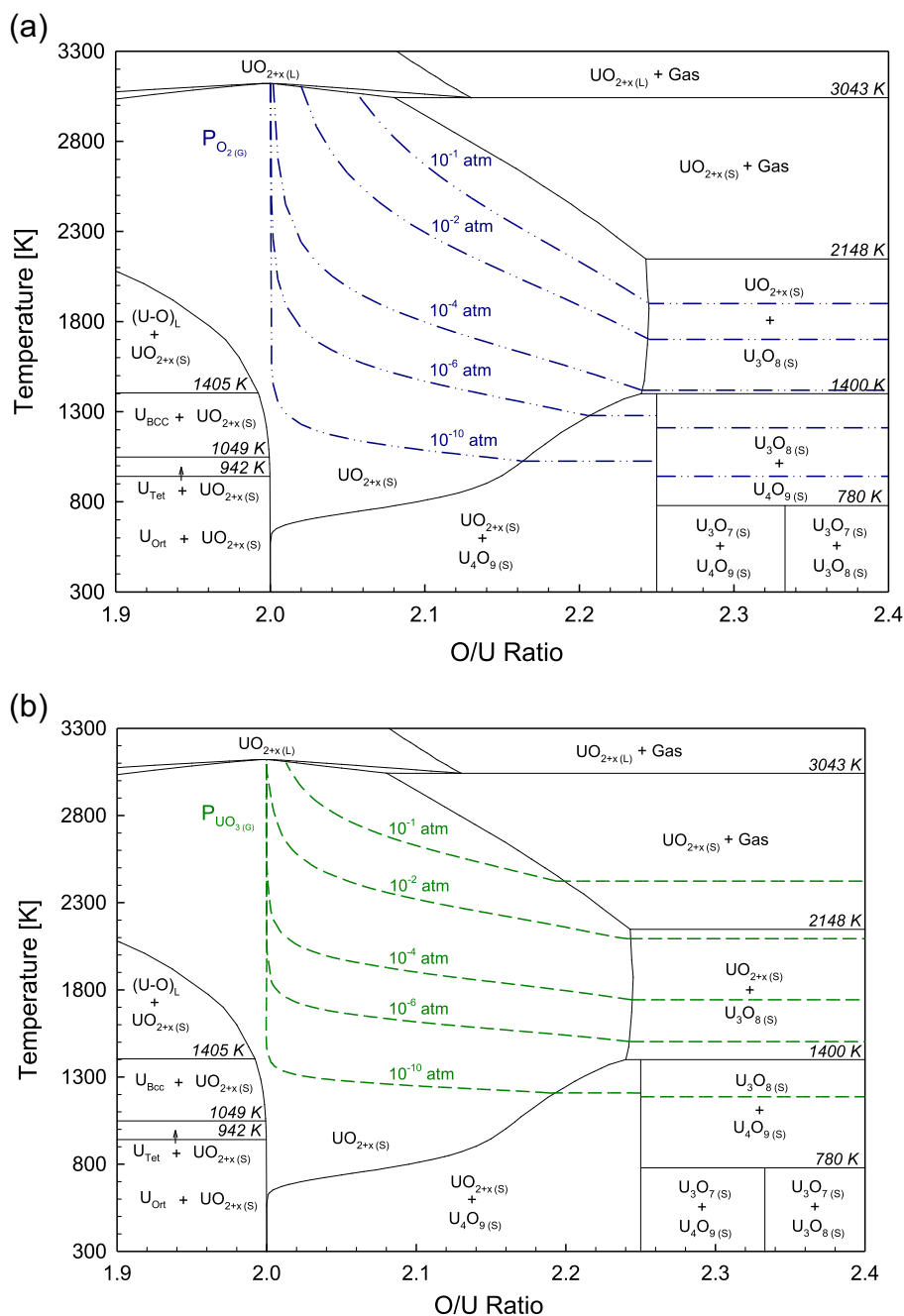


Fig. 10 Calculated U–O binary phase diagram with isobaric lines of (a) oxygen and (b) UO_3 partial pressure. Reproduced from Piro, M.H.A., 2011. Computation of Thermodynamic Equilibria Pertinent to Nuclear Materials in Multi-Physics Codes. PhD Thesis. Kingston: Royal Military College of Canada.

for irradiated fuel, encompassing the complex U–O system, and the fission product and actinide components, as briefly described in Sections 2.07.3.2.1–2.07.3.2.4.

2.07.3.2.1 Solutes in UO_2

Table 4 shows the various oxides contained in **Fig. 6** that can be found as solutes in uranium dioxide. Kleykamp⁶⁵ has reviewed data for 12 oxides dissolved in UO_2 . In a typical experiment involving, for example, Cs_2O , two samples of near stoichiometric powdered UO_2 ($\text{O/U} = 2.003$) were mixed with Cs_2O inside a thoria crucible. These crucibles were sealed within separate tantalum capsules, as shown in **Fig. 12**. Each assembly was annealed at either 1273 or 2173K for 8 h. The experiment at the lower temperature did not attain thermodynamic equilibrium,² but the results at 2173K yielded the following observations: (1) the

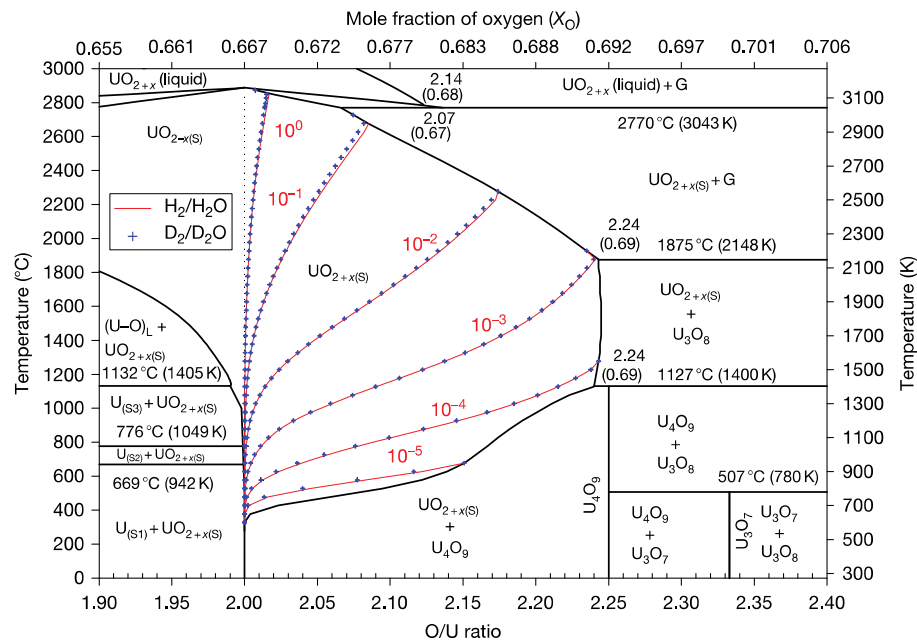


Fig. 11 Calculated U–O binary phase diagram with lines of constant H_2/H_2O and points of constant D_2/D_2O ratios as calculated from Eqs. (3) and (4).

Table 4 Oxides (grouped by O/M proportion) included as solutes in UO_2

M_2O	MO	M_2O_3	MO_2
Cs_2O	SrO	Ce_2O_3	CeO_2
Rb_2O	BaO	Dy_2O_3	MoO_2
		Ho_2O_3	NbO_2
		La_2O_3	NpO_2
		Nd_2O_3	PuO_2
		Pr_2O_3	TeO_2
		Sm_2O_3	ZrO_2
		Y_2O_3	

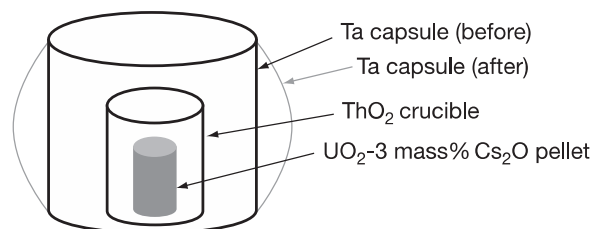


Fig. 12 Schematic diagram of Cs_2O “solubility” experiment.

internal pressure of the Ta capsule was estimated to be 200 bar from the wall curvature; (2) a tantalum oxide layer deposited on the inner walls of the Ta capsule; and (3) the level of dissolved Cs in the pellet was 0.08 mol% Cs_2O .

This experiment does not give the solubility of Cs_2O directly, that is, Cs_2O dissociates, oxygen combines with Ta, and a high Cs vapor pressure causes the capsule to swell. All of these factors must be considered in extracting the required thermodynamic data for Cs_2O dissolved in a UO_2 solid solution. The inferred Gibbs energy change for



as well as for other oxides is given in Table 5. Note that the number of moles of foreign solute cations per formula mass is also given. When the Gibbs energy of mixing equations is formulated, the mole fractions of the solute oxide are based on a formula

Table 5 Thermodynamic data for selected solute oxides in UO_2

Oxide	Solubility in UO_2 (mol%)	Temperature (K)	Excess Gibbs energy (w.r.t. solid) (J mol^{-1})	Cations per formula mass
Cs_2O		2173	230	2
La_2O_3	69	523	$-2686 + 8.505T$	2
La_2O_3	50	1523		2
Pr_2O_3	55	1523	$-4268 + 8.505T$	2
Nd_2O_3	68	1523	$-7714 + 8.505T$	2
PuO_2	Miscible	0	1	
NpO_2	Miscible	0	1	

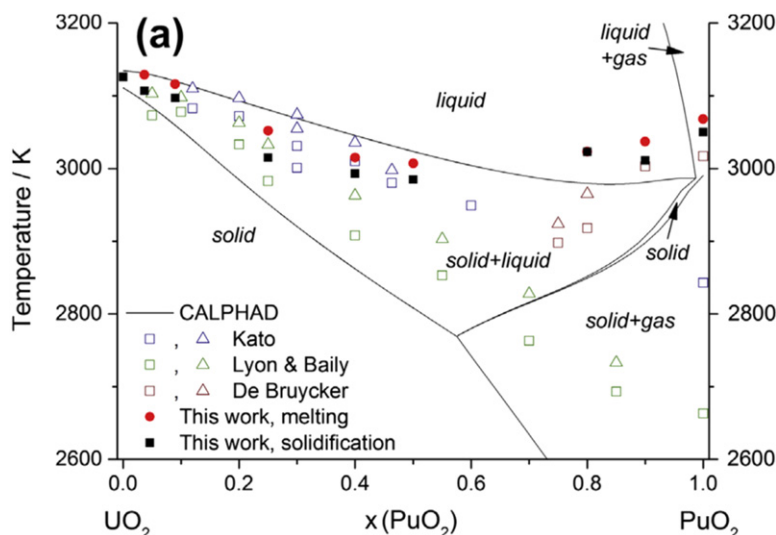


Fig. 13 The UO_2 – PuO_2 phase diagram, according to Böhler *et al.* The solid lines correspond to calculated values from a thermodynamic treatment and symbols represent experimental data points. Reproduced from Böhler, R., Welland, M.J., Prieur, D., *et al.*, 2014. Recent advances in the study of the UO_2 – PuO_2 phase diagram at high temperatures. *J. Nucl. Mater.* 448, 330–339.

mass containing only one mole of the metal. Solubility data along with the inferred Gibbs energy changes for selected lanthanide sesqui-oxides also appear in Table 5.

The behavior of PuO_2 in relation to its dissolution in UO_2 may be inferred from the phase diagram in Fig. 13.^{66–68} Although there is a divergence on the melting of pure PuO_2 , all studies indicate complete miscibility of PuO_2 in UO_2 in both the solid and liquid phases.^{69,70} There remains some uncertainty in the precise melting behavior of the UO_2 – PuO_2 pseudo-binary system, as evidenced by the divergent trends shown in Fig. 13. Similar melting experiments of the UO_2 – NpO_2 pseudo-binary system has been performed by Belyaev⁷¹ and Chikalla.⁷²

2.07.3.2.2 Noble metals

The presence of noble metal inclusions (the so-called “white phase” or “five metal” inclusions) in irradiated fuel is well documented.^{5,73–79} Thermodynamic models for these inclusions have been developed.^{17,80} The insufficiency of oxygen to combine with the chemically more noble metallic fission products creates an alloy phase of Pd, Rh, Ru, Mo, and Tc. Four calculated isothermal (1973K) ternary phase diagrams are shown in Fig. 14. The triangles are arranged so that Rh–Pd, Rh–Ru, and Pd–Ru binary edges on the central triangle are common to the edges of the surrounding three ternary systems involving Mo. Fig. 15 illustrates how the central ternary system is related to its binary subsystems.

2.07.3.2.3 Non-fluorite oxide phases

Separate oxide phases are known to appear in irradiated fuel.⁸¹ Oxide inclusions of the type $(\text{Ba}, \text{Sr})(\text{U}, \text{Pu}, \text{Zr}, \text{Mo})\text{O}_3$ form a “gray” phase with a perovskite structure, and result because of the extremely limited solubility of BaO and SrO in actinoid oxides. The presence of zirconium generally leads to the formation of zirconates.

Four distinct minor solid oxide phases and one liquid oxide phase can be considered for the thermodynamic model¹⁵: (1) (Rb/Cs) zirconate solid – $(\text{Rb}, \text{Cs})_2\text{ZrO}_3$; (2) (Sr/Ba) zirconate solid – $(\text{Sr}, \text{Ba})\text{ZrO}_3$; (3) (Rb/Cs) uranate solid – $(\text{Rb}, \text{Cs})_2\text{UO}_4$; (4) (Sr/Ba) uranate solid – $(\text{Sr}, \text{Ba})\text{UO}_4$; and (5) (Rb/Cs) molybdate liquid – $(\text{Rb}, \text{Cs})\text{MoO}_4$. The mixing treatments recognize the number of moles of ions contributed to the solid solution in relation to the formula mass of the

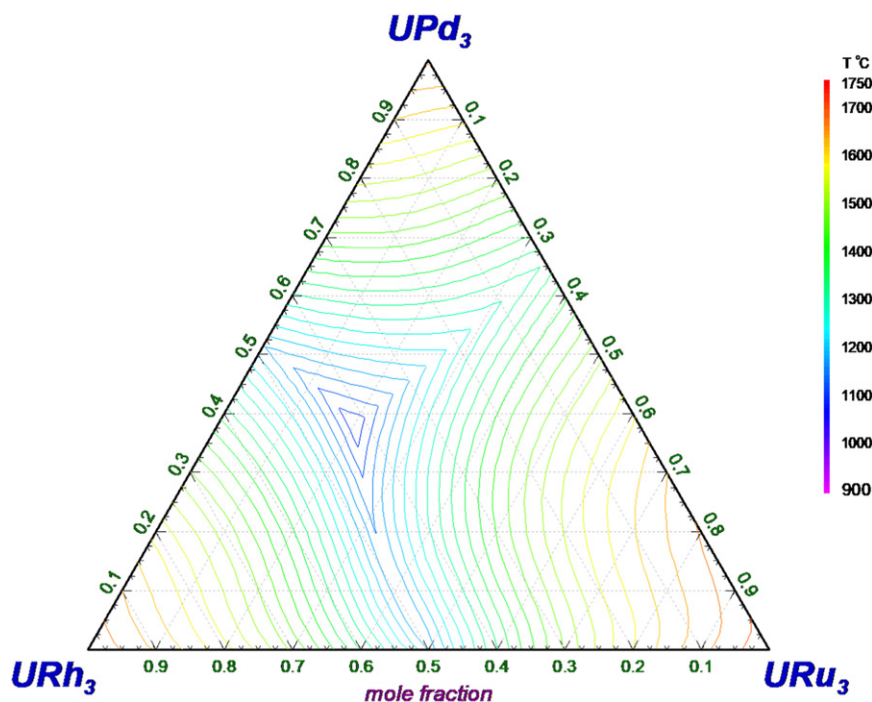


Fig. 16 A calculated pseudo-ternary liquidus projection is shown for the UPd_3 - URu_3 - URh_3 system. Reproduced from Wang, L.C., 2018. Developing a Thermodynamic Model for the U-Pd-Rh-Ru Quaternary System for Use in the Modelling of Nuclear Fuel. PhD Thesis. Oshawa: University of Ontario Institute of Technology.

three solid compounds UPd_3 , URh_3 , and URu_3 ,¹⁵ the data for which can be derived from Cordfunke and Konings.⁸⁶ Wang provided a detailed thermodynamic description of the pseudo-binaries, which provide a foundation for the pseudo-ternary system.⁸⁷ Fig. 16 shows the calculated liquidus projection of this pseudo-ternary system.⁸⁷

2.07.3.2.5 Establishing the fuel inventory for equilibrium calculations

The fission product inventory for any particular fuel, at a given burnup in-reactor or during storage, may be calculated by a depletion, decay and transmutation code, such as ORIGEN.⁸⁸ Fig. 4 gives an example calculation of the fission product inventory in PWR fuel. The majority of these elements are present in very small concentrations. To simplify the calculations, most thermodynamic calculations typically consider less than ~20 chemical elements – the most important ones being ranked both by relative concentration (e.g., Pu, Zr, and Mo) and by the radiological consequences (e.g., I, Cs, Xe, and Ru). In addition, oxygen and hydrogen can be added to the thermodynamic calculation to allow for the possible presence of steam in the event of a cladding breach.

2.07.3.2.6 Irradiated fuel system

Following the CALPHAD method, one can assemble the individual binary and ternary sub-systems to establish a larger multi-component system representing irradiated UO_2 nuclear fuel. In such a treatment, the U-O system provides the foundation – particularly a model for $\text{UO}_{2\pm x}$ (Section 2.07.3.1) – with additional fission product systems, which provides a mechanism to determine the solubility of fission products in the UO_2 fluorite structure and secondary phases that can form (e.g., as per Sections 2.07.3.2.2–2.07.3.2.4). Fig. 17 gives an example of the predicted phase assemblage varying with respect to oxygen content of a highly irradiated PWR fuel corresponding to the rim region of Walker *et al.*⁸⁹ In this system, UO_2 solid solution is stable over a wide range of oxygen content, but it is worth noting that several other phases are predicted to be stable in Fig. 17. The noble metal phase with a hexagonal closed-packed crystal structure (Pearson symbol hP2) is stable over a wide range of oxygen content, while other noble metal phases (e.g., cI2) and perovskite phases are stable as well. Gas was excluded from the calculation, which was predominantly xenon and krypton, which are inert anyway and do not chemically interact with the other sub-systems.

The effects of irradiation from the calculations shown in Fig. 17 on oxygen partial pressure in equilibrium with the fuel is illustrated in Fig. 18. Note that the abscissa plots the oxygen to metal ratio of the entire fuel (i.e., fluorite phase and secondary phases), whereby fission product elements are divided by two with the intent of capturing an equivalent approximation of the initial actinoid content. The intent is to provide a more comparable just a position to the fresh fuel, which is also shown in Fig. 18. As is clearly demonstrated, the oxygen partial pressure is greatly affected by irradiation in both magnitude and curvature. The change in curvature of the irradiated fuel is associated with phase changes that occur, which can be made in reference to Fig. 17.

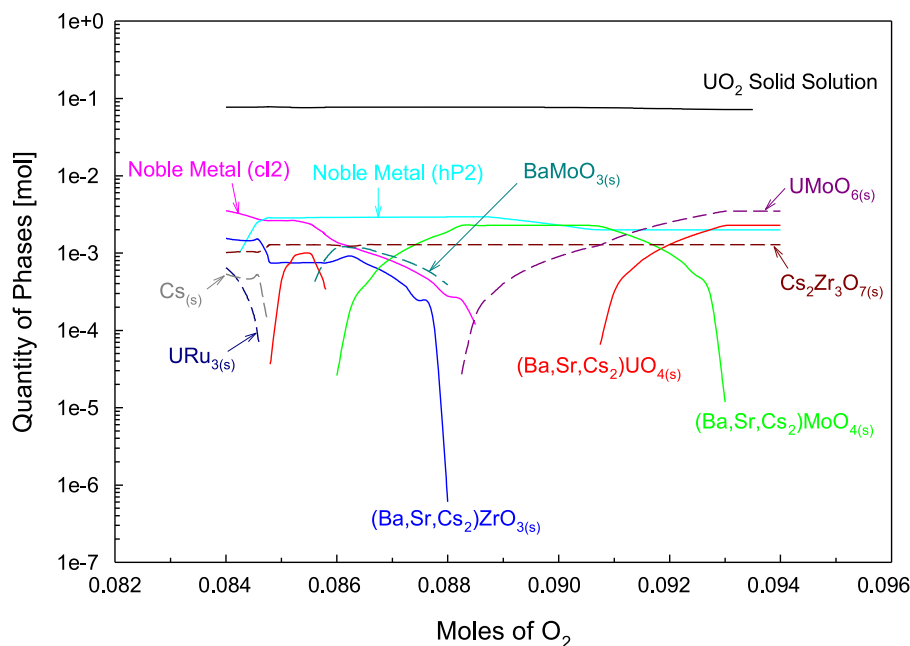


Fig. 17 The predicted quantities of all phases are shown in relation to the number of moles of oxygen for PWR fuel with a burnup of 158 GWd/t (U) (corresponding to the rim region of high burnup fuel, after Walker *et al.*). Reproduced from Piro, M.H.A., 2011. Computation of Thermodynamic Equilibria Pertinent to Nuclear Materials in Multi-Physics Codes. PhD Thesis. Kingston: Royal Military College of Canada. Walker, C.T., Rondinella, V.V., Papaioannou, D., *et al.*, 2005. On the oxidation state of UO_2 nuclear fuel at a burn-up of around 100 MWd/kgHM. J. Nucl. Mater. 345, 192–205.

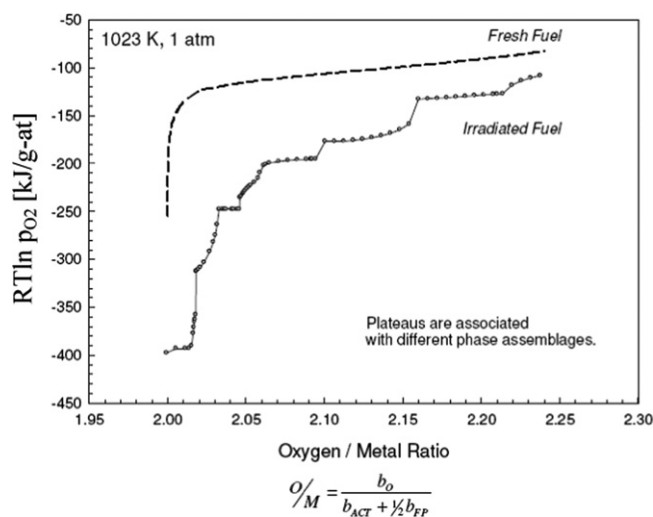


Fig. 18 Variation in oxygen partial pressure ($RT \ln p_{\text{O}_2}$) with respect to oxygen to metal ratio comparing fresh fuel to highly irradiated PWR fuel. The plateaus in the irradiated fuel profile correspond to phase changes. Reproduced from Piro, M.H.A., 2011. Computation of Thermodynamic Equilibria Pertinent to Nuclear Materials in Multi-Physics Codes. PhD Thesis. Kingston: Royal Military College of Canada.

The Thermodynamics of Advanced Fuels – International Database (TAF-ID) project, coordinated by the Organization for Economic Co-operative Development Nuclear Energy Agency (OECD/NEA), started in 2013 as a collaboration between six countries (Canada, France, Japan, Netherlands, Republic of Korea, and USA) with the objective to develop and improve a thermodynamic database for a wide range of applications in the field of nuclear materials.^{90,91} The two main applications in the nuclear industry are aiding lifetime extension of existing Generation II-III reactors, and the development of Generation IV reactors.

The database is built on the basis of the Calphad technique,^{92–94} which, based on experiments and/or ab initio calculations, models each possible phase in terms of Gibbs energy as a function of temperature, pressure, and composition. The description of the fluorite $(\text{U,Pu})\text{O}_2$ phase is based on the work of Guéneau *et al.*,⁶¹ which used the Compound Energy Formalism (CEF). Thus, the oxide fuel in solution with its fission products can in this case be written as $(\text{Al}^{3+}, \text{Am}^{3+}, \text{Am}^{4+}, \text{Ca}^{2+}, \text{Ce}^{3+}, \text{Ce}^{4+}, \text{Gd}^{3+},$

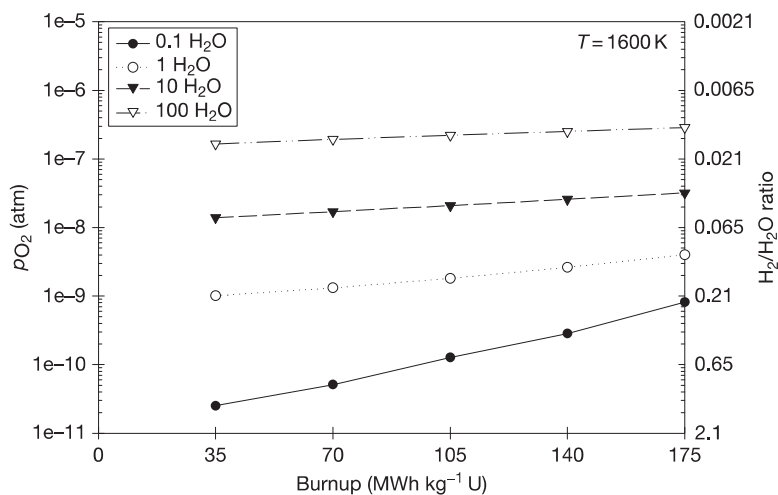


Fig. 19 Oxygen partial pressure for various amounts (moles) of steam for a typical CANDU fuel element with burnup.

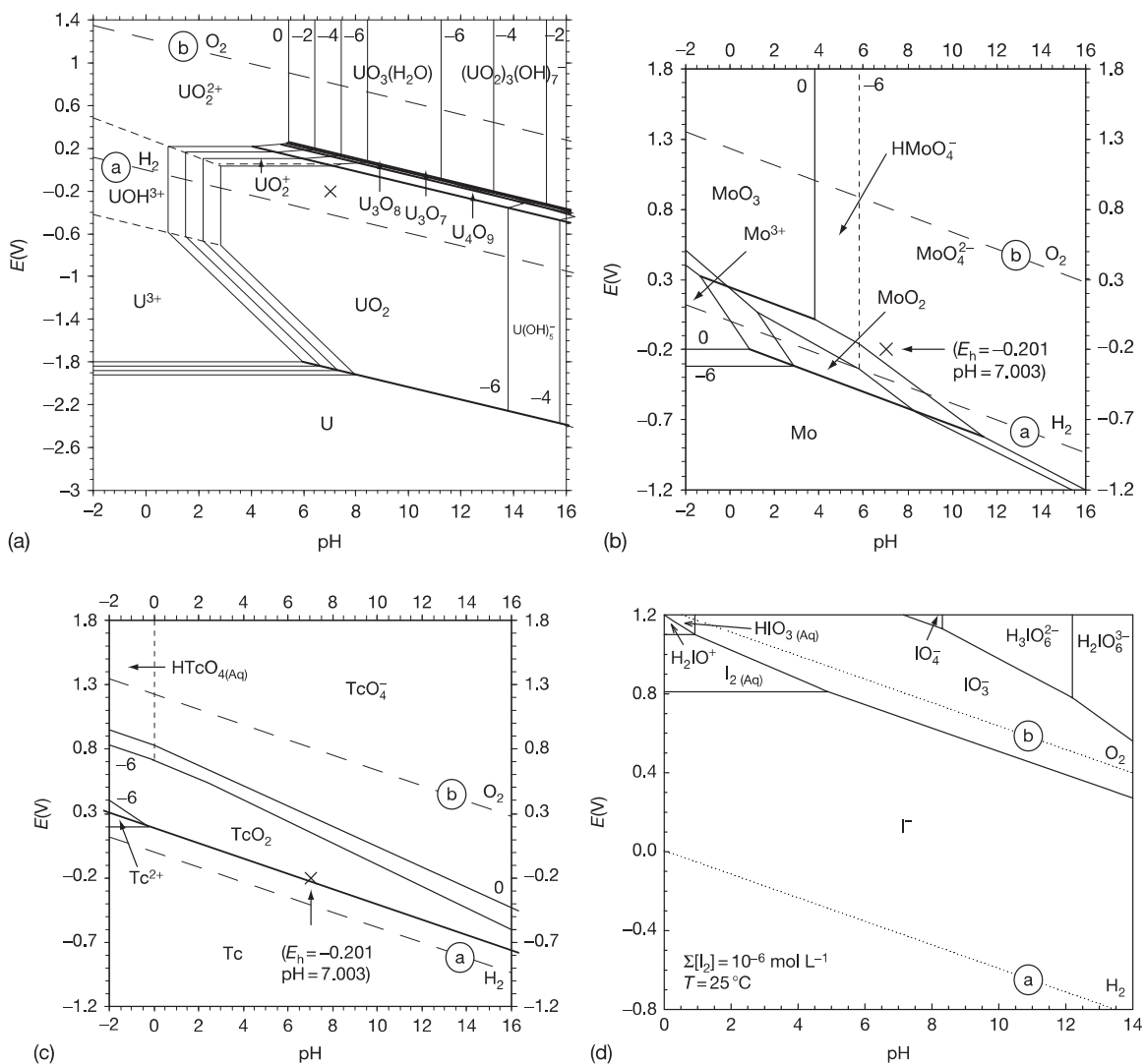


Fig. 20 Computed Pourbaix diagrams at 298.15 K for (a) U-H₂O, (b) Mo-H₂O, (c) Tc-H₂O, and (d) I-H₂O. (d). Modified from Ticknor, K.V., Cho, Y.H., 1990. J. Radioanal. Nucl. Chem. 140, 75–90.

La^{3+} , Mg^{2+} , Nb^{5+} , Nd^{3+} , Np^{3+} , Np^{4+} , Pu^{3+} , Pu^{4+} , Th^{4+} , U^{3+} , U^{4+} , U^{5+} , Zr^{2+} , Zr^{4+}) $(\text{O}^{2-}, \text{VA})_2$ $(\text{O}^{2-}, \text{VA})$, where VA indicates a vacancy.

The liquid phase is described using the partially ionic two-sublattice liquid model.^{95,96} Here, the first sublattice is occupied by cations, and the second by anions, “hypothetical vacancies” and neutral species. This allows for both purely metallic, and ionic liquids to be simulated by the same model. This means that only for these ternaries, ternary interactions are introduced whereas the other ternaries are calculated by extrapolating the binary sub-systems.

2.07.4 Defective Fuel Behavior

With the occurrence of defective fuel, coolant can enter the fuel element and react with the oxide fuel and cladding. It is important to understand fuel oxidation phenomena with defective fuel operation since hyperstoichiometric UO_2 has a reduced thermal conductivity and a lower incipient melting temperature (corresponding to the solidus), which can both negatively affect the thermal performance of the fuel rod while reducing the margin to fuel centerline melting.²² In addition to fuel oxidation phenomena, fission products (i.e., notably the volatile species of noble gas and iodine) will be released into the primary coolant.^{97–99} Moreover, the fission product diffusivity is enhanced with continued fuel oxidation.^{12,99,100} Thermochemical models can be employed to predict the equilibrium state of the oxidized fuel (i.e., fuel oxygen potential) for defective fuel analysis (Section 2.07.4.1). The understanding of the aqueous chemistry of the fuel and fission product system is needed to assess the potential for the leaching of fission products from defective fuel during reactor shutdown as well as the impact of defective fuel storage in the water bays (Section 2.07.4.2).

2.07.4.1 Fuel Oxidation Phenomena

With the knowledge of the equilibrium stoichiometry deviation x_e in Eqs. (4) or (5), the kinetics of fuel oxidation can be described where the fuel oxidation reaction will cease when the stoichiometry deviation x in UO_{2+x} reaches the equilibrium value.^{101,102} Consequently, interstitial transport of oxygen in the defective element for the stoichiometry deviation x can be determined from the mass balance equation²²:

$$\frac{\partial x}{\partial t} = \vec{\nabla} \left(D \left(\nabla_x + x \frac{Q}{RT^2} \nabla T \right) \right) + \sigma_f \alpha \sqrt{p\text{H}_2\text{O}} (x_e - x) \quad (7)$$

Here σ_f is the surface area of cracks per unit volume of fuel for the cracked fuel pellet, D is the chemical diffusion coefficient for the oxygen interstitials, Q is the effective molar heat of transport, α is the rate coefficient for the surface exchange of oxygen at the fuel/atmosphere interface,¹⁰¹ and $p\text{H}_2\text{O}$ is the partial pressure of H_2O . Using Eq. (7), the oxygen-to-uranium (O/U) ratio and its distribution within the pellets can therefore be predicted as a function of the post defect residence time. This computation involves the simultaneous consideration of the gas phase transport of hydrogen and steam in the fuel-to-clad gap and fuel cracks, and the heat transfer in the fuel pellets accounting for the dependence of thermal conductivity on the degree of fuel oxidation.²² The O/U radial profiles predicted using Eq. (7) are in good agreement with measurements obtained from commercial defective fuel elements of the oxygen-to-metal (O/M) ratio.

The oxygen partial pressure calculations in Eqs. (4) and (5) are applicable only for fresh fuel, whereas, with irradiation, fission products and actinides are produced. The fission product elements may form compounds with oxygen that will affect the oxygen potential within the fuel, as shown in Fig. 18. The advantage of the more general computational thermodynamics approach is that the U–O thermodynamic treatment can be extended to include fission products and actinides, in comparison to earlier correlations of oxygen potential (e.g., the Lindemer and Besmann treatment⁶²) to assess the impact of fuel burnup. For instance, as shown in Fig. 19, for a typical discharged burnup of ~ 175 MWh per kilogram of U for CANDU fuel reacting in the presence of increasing amounts of moles of steam, such calculations show that the effect of fission products on the fuel oxygen potential is small for the expected hydrogen-to-steam partial pressure ratio in Fig. 11. While this may be true for CANDU fuel where burnup is low, this is generally not the case in PWR fuel where burnup is much higher.

2.07.4.2 Aqueous Fuel and Fission Product Behavior

“Iodine-spiking” phenomenon can occur during reactor shutdown when the temperature in the fuel-to-clad gap drops below the steam saturation temperature, permitting liquid water to dissolve the soluble iodine species in the gap.^{103–105} To better understand the fission product leaching behavior during reactor shutdown, a further thermodynamic analysis can be performed assuming that either a vapor or aqueous phase is present in the fuel-to-clad gap (Table 6). The fission products that readily dissolve in the water and are subsequently washed out of the fuel-to-clad gap from a defective element during shutdown or startup operation include Cs ($\text{Cs}^+ + \text{I}^-$), Mo ($\text{MoO}_4^{2-} + \text{I}^-$), iodine ($\text{I}^- + \text{I}_2$), and Rb ($\text{Rb}^+ + \text{I}^-$), while the fission products that are not expected to wash out are Zr, Ba, La, (and other Ln), Rh, Ru, Sr, Tc, and Te. It is for this reason that the concentration of La is used to infer the burnup of the

Table 6 Fission product inventory modes of formation with only a vapor phase and an aqueous phase present in the fuel-to-clad gap

Fission product	Vapor phase present in the fuel-to-clad gap		Aqueous phase present in the fuel-to-clad gap		
	Solid	Vapor	Solid	Vapor	Aqueous
Xe (10% Kr)	No formation	Entire inventory	No formation	Entire inventory	No formation
Cs	Cs ₂ MoO ₄ CsI	No formation	No formation	No formation	Cs [+]
Mo	MoO ₂ (in UO _{2+x}) Cs ₂ MoO ₄ Rb ₂ MoO ₄	No formation	MoO ₂ (in UO _{2+x})	No formation	MoO ₄ [2 –]
Zr	SrZrO ₃ ZrO ₂	No formation	SrZrO ₃	No formation	No formation
I	CsI	No formation	No formation	No formation	I [–]
Ba	BaUO ₄	No formation	Ba(OH) ₂ BaUO ₄	No formation	No formation
Rb	Rb ₂ MoO ₄	No formation	No formation	No formation	Rb [+]
La	La ₂ O ₃ (in UO _{2+x})	No formation	La ₂ O ₃ (in UO _{2+x})	No formation	No formation
Rh	hP2 – noble metal inclusion	No formation	hP2 – noble metal inclusion	No formation	No formation
Ru	hP2 – noble metal inclusion	No formation	hP2 – noble metal inclusion	No formation	No formation
Sr	SrZrO ₃	No formation	SrZrO ₃	No formation	No formation
Tc	hP2 – noble metal inclusion	No formation	hP2 – noble metal inclusion	No formation	No formation
Te ^a	TeO ₂ (in UO _{2+x})	No formation	TeO ₂ (in UO _{2+x})	No formation	No formation

^aFindings are subject to further investigation.

Note: hP2, hexagonal – primitive (with two atoms in the unit cell).

fuel during post-irradiation examination. The presence of Zr, Ba, La, Rh, Ru, Sr, and Tc in the coolant is therefore evidence of fuel debris in the coolant system. These predictions are in qualitative agreement with the observed leaching behavior in in-reactor loop experiments¹⁰⁶; however, in contrast to the thermodynamic prediction, which suggests that Te remains as TeO₂ dissolved in the UO_{2+x}, the loop experiments indicate that Te is released out of high power defected fuel elements during shutdown conditions. This matter warrants further inquiry since the washout of ¹³²Te becomes an important issue when determining the ¹³²I coolant activity behavior on shutdown.⁹⁹

Spent defective fuel bundles are eventually stored for long periods (i.e., several years) in water bays at ~30°C. The water bays are oxygenated since they are open to the air surface and are therefore virtually in equilibrium with the air. The thermodynamic treatment described in Section 2.07.3 can be further applied to understand the fuel oxidation behavior in the storage bays. In this case, the diagrams of Pourbaix originally developed to better understand aqueous corrosion phenomena are helpful. The diagrams of redox potential, E_h , versus pH are an important method for understanding aqueous chemical behavior.¹⁰⁸ The redox potential is the conventional electrometric way of expressing the oxidizing ability of the solution in place of giving the oxygen partial pressure at a particular pH. The uranium Pourbaix diagram at 298K, covering the range of redox potential pertinent to fuel oxidation behavior, is shown in Fig. 20(a). The details of the diagram development via Gibbs energy minimization are given in Lewis.¹⁰⁹ The data for UO₂, U₄O₉, U₃O₇, and U₃O₈ are the same as those used for the U–O binary phase diagram in Fig. 10. Placed on the diagram for reference are dashed lines (a) and (b) corresponding to redox potentials associated with hydrogen and oxygen saturation (at 1 atm partial pressure), respectively. This methodology provides a means to assess fuel oxidation behavior of defective fuel during long-term storage in the fuel bays.

Furthermore, similar diagrams can also be developed to better understand the aqueous behavior and leaching of such fission products as Mo and Tc (Fig. 20(b) and (c), respectively).¹⁰⁹ In the case of iodine, as shown in Fig. 20(d), the diagram has been reconstructed from the work of Ticknor and Cho.¹¹⁰ Note that solid iodine does not appear as a field in Fig. 20(d) since the concentrations for the aqueous species fields were constructed for 10^{–6} molar. Since the redox potential of the water will be controlled by the UO₂ water reactions shown in Fig. 20(a), the condition marked by x in Fig. 20(a) (established by independent computations) can be used to locate the relevant field in Fig. 20(b)–(d). For example, for CANDU coolant conditions during reactor shutdown, Mo would be expected to oxidize principally to MoO₄^{2–} ions, while the concentrations for the aqueous species of Tc would be undetectable. Thus, if Tc were detected in the coolant water phase, it could arise (since there is an absence of dissolved oxygen) only as a result of the decay of Mo.¹⁰⁹ In the case of iodine, it is evident from Fig. 20(d) that I[–] is, practically speaking, the only water-soluble iodine species at any pH in the absence of air. The IO₃[–] field of stability is only reached near conditions of air saturation (near line (b)).

Experiments conducted in aerated water for ~20 days at ~200°C with uranium dioxide fuel specimens have indicated that fuel oxidation can occur via (1) solid-state diffusion to U₃O₇ (similar to dry oxidation), (2) oxidative dissolution and precipitation of U(VI) as ~ (UO₃) · 0.8H₂O, and (3) back-reduction of dissolved U(VI) on the UO₂/U₃O₇ surface to form U₃O₈.¹¹¹ These species are consistent with the computed Pourbaix diagram in Fig. 20(a) that shows the dissolution/precipitation product UO₃(H₂O).

As was shown in Fig. 20(a), nearly pure UO_2 has fairly low solubility in water under the electrochemical conditions typically maintained in-reactor. However, this is not the case for several of the transuranic. This is demonstrated in Fig. 21, which gives the Pourbaix diagrams of the $\text{U-H}_2\text{O}$, $\text{Np-H}_2\text{O}$, $\text{Pu-H}_2\text{O}$, $\text{Am-H}_2\text{O}$, and $\text{Cm-H}_2\text{O}$ systems at 550K.¹¹² Of particular importance is the higher degree of solubility of curium in water, which may be problematic in the event of component discharge from the reactor or possibly the leaching out of solution under deep geological repository conditions.

2.07.5 High-Temperature Fuel and Fission Product Behavior Under Accident Conditions

To better understand the integral effects of fission product release under degraded core conditions, numerous in-pile experiments have been conducted (e.g., Source Term (ST) tests, Source Term Experiments Project (STEP) tests, Power Burst Facility (PBF) Severe Fuel Damage (SFD) tests, Full Length High-Temperature (FLHT) tests, Loss-of-Fluid Test Facility (LOFT) Fission Product (FP-2) test, Knudsen Effusion Mass Spectroscopy (KEMS),¹⁰⁷ and the Phebus Fission Product Tests (FPT)), including an examination of core material following the Three Mile Island Unit 2 (TMI-2) accident.^{31,113,114} In addition, out-pile annealing tests conducted at high temperatures with spent fuel samples in various environments provided an additional opportunity to study separate effects behavior (e.g., Horizontal Induction (HI) and Vertical Induction (VI) test series at the Oak Ridge National Laboratories (ORNL), the Heva, Vercors and Verdon test series at the Commissariat à l'Energie Atomique (CEA), and the Verification Experiments of radionuclides Gas/Aerosol release (VEGA) program at the Japan Atomic Energy Agency (JAEA)).^{31,115} Typical results from these various experiments are summarized in Table 7. Details of the various in- and out-pile experiments are given by Lewis.³¹ An informative overview of release mechanisms from a severe accident is provided by Konings *et al.*¹¹⁶

The fission product releases from the in-pile PBF tests (i.e., SFD-ST (steam-rich), SFD 1-1 (steam-starved), and SFD 1-4 (steam-starved)), and Phebus FPT-1 test (steam-rich) are compared with those in the TMI-2 accident shown in Table 7.^{31,117,118} These results indicate very low release fractions for cerium and the actinoids (typically <0.01%); ruthenium, strontium, and antimony generally <1%; barium less than a few percent; molybdenum up to 50%; similar volatile release behavior of iodine, cesium, and noble gases up to ~90%; and tellurium between 1% and 83%. These findings are also consistent with those observed for annealing experiments. However, there is a difference for the barium release between the in-reactor Phebus FPT-0 and FPT-1 experiment (~1%) and the HI, VI, and Vercors annealing tests (>40%) (see Table 8).¹¹⁹ This difference is thought to be attributed to (1) the short duration of the temperature escalation in the in-pile tests, where there is no "high-temperature plateau" as in the annealing tests but rather a temperature escalation due to the formation of a molten pool in the Phebus experiment; and (2) the presence of a significant amount of ZrO_2 in the fuel melt (~47mol%) as well small amounts of iron oxide in the in-reactor test which can reduce the volatility of Ba.¹¹⁹ Moreover, thermochemical calculations suggest that the Ba vapor pressure is reduced in the solidus-liquidus transition zone as shown in the U-Ba-O phase diagram (~2400–3100K).¹¹⁹ Release rates of volatile fission products were large during the temperature escalations in the PBF SFD 1-1 and 1-4 tests and the Phebus FPT-0 test. In the Phebus FPT-0 test, the highest mass flow rates of aerosol and fission products (i.e., ^{131}I , ^{139}Xe , ^{140}Xe , ^{90}Kr , and ^{92}Kr), as well as structural materials (such as tin, silver, and indium), were observed at a peak temperature of ~2770K.

The oxygen potential plays an important role, principally in the release characteristics of the low-volatile fission products. Only small releases of barium and strontium are observed in the steam experiments of Table 7 as the prevailing atmosphere typically hindered the formation of the more volatile metallic species but favored low-volatility oxides and hydroxides²⁹; in fact, releases for these species occurred in the Phebus FPT-0 test during the temperature escalation phase when hydrogen generation was at a maximum.¹²⁰ This observation is consistent with the in-pile ST experiments, where higher releases of several percent for barium and strontium, and up to 15% for europium, were observed in a reducing environment which would promote more volatile forms of these species.¹²¹ These results are also seen in the VI, Heva, and Vercors annealing tests.^{122,123} Since ruthenium-ruthenium oxide has the highest oxygen potential of all fission products (see Fig. 5), the higher-volatile oxides cannot form for the given steam-hydrogen mixtures of the experiments shown in Table 7 or in the TMI-2 accident.

As indicated in Table 7, the tellurium release is dependent on the extent of Zircaloy oxidation, where large releases occur when the Zircaloy cladding is nearly completely oxidized. Although tellurium is released from the fuel on heating, it will chemically react with the Zircaloy cladding and become trapped.^{9,28,124,125} During Zircaloy oxidation, the tin constituent in the cladding is segregated as a thin band in the zirconium oxide layer, which advances with the metal-oxide interface, because of the lower solubility of Sn in the oxide than in the metal (and its placement relative to Zr on the Ellingham diagram shown in Fig. 5). After complete oxidation, there is a production of elemental tellurium and zirconium oxide from the reaction of zirconium telluride with oxygen; however, as a consequence of the tin segregation process, an enhanced formation of SnTe ultimately leads to a release of tellurium. A SnTe compound has in fact been observed by Collins *et al.* under accident conditions.¹²⁶ Only at high oxygen partial pressures, which are above the equilibrium value of Sn/SnO_2 , as shown in Fig. 5, will tellurium be released in its elemental form. This delayed release behavior for tellurium has been observed in numerous annealing experiments.¹²⁷ Significant tellurium release occurred in the Phebus FPT-0 and FPT-1 tests because of the extent of cladding oxidation. Although antimony, like tellurium, is readily released from the fuel during heating in a severe accident, a lower release is observed since the antimony most likely sequesters in metallic melts (as it alloys with other metals such as nickel and silver).

In Table 7, comparison of the volatile releases for the comparable tests, PBF SFD 1-1 and 1-4, indicates that the release is enhanced in high-burnup fuel compared to trace-irradiated fuel because of the presence of grain boundary tunnels that serve as pathways for gaseous release. Enhanced release rates (due to fuel morphology) occur primarily during the initial heating, while

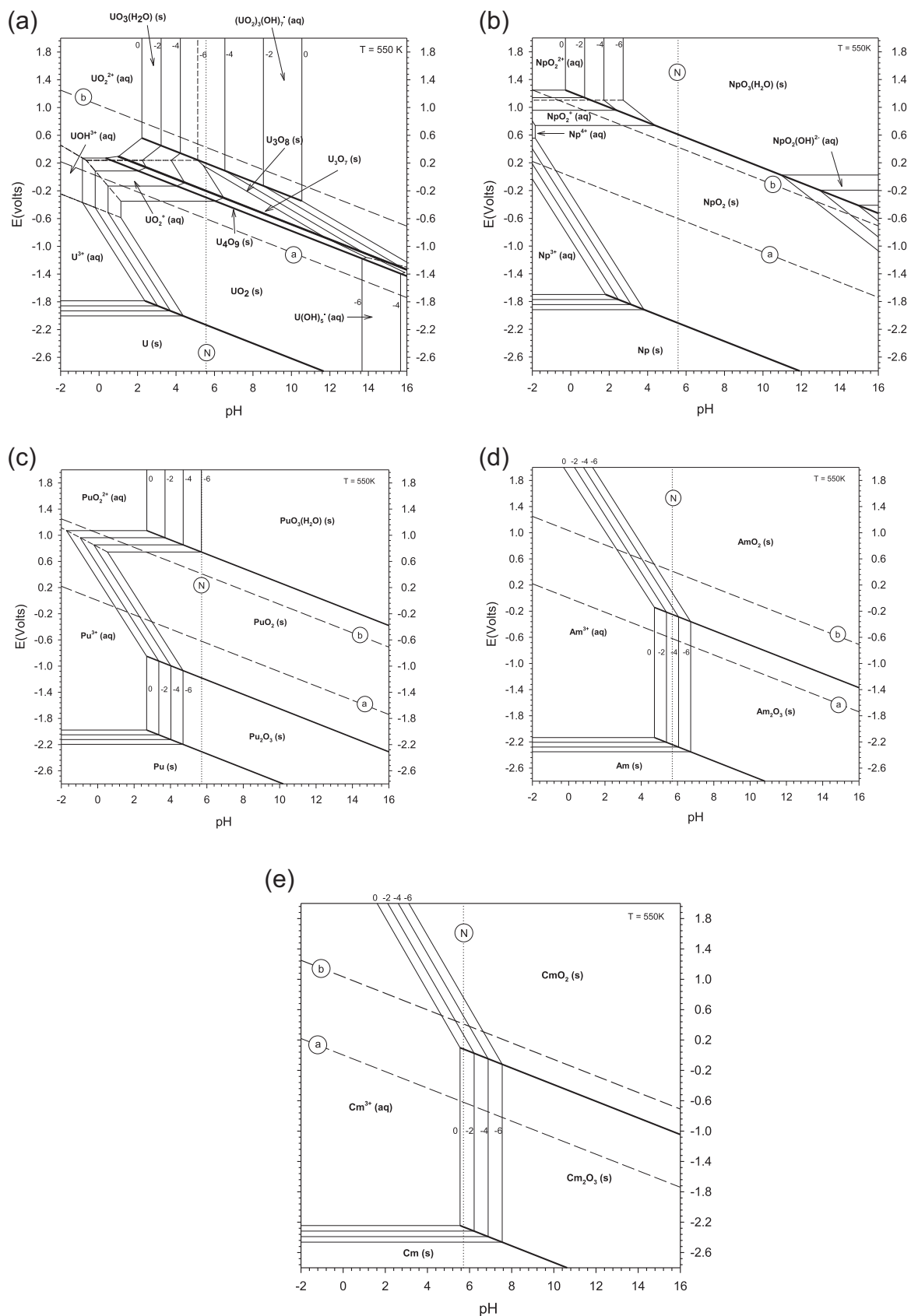


Fig. 21 Computed Pourbaix diagrams of the U-H₂O, Np-H₂O, Pu-H₂O, Am-H₂O, and Cm-H₂O systems at 550K. Reproduced from Piro, M.H., Bruni, G.M.F., Lewis, B.J., *et al.*, 2010. Computation of Actinide Pourbaix Diagrams at 298 and 550K (U,Np,Pu,Am,Cm – H₂O). In: Proceedings of the 11th International Conference on CANDU Fuel. Niagara Falls, ON.

Table 7 Comparison of fission product release fractions from in- and out-pile experiments and TMI-2^a

Element and experimental conditions	Fission product release fractions (%)									
PBF experiments	SFD 1–1		Phebus	TMI-2		Annealing ORNL and VI tests				
SFD-ST	SFD 1–1	SFD 1–4	FPT-0	FTP-1	VI-3	VI-5	Vercors-4	Vercors-5		
T_{\max} (K)	2800	2800	2800	~2870	2500	2800	2700	2720	2570	2570
Atmosphere	H ₂ O	H ₂ O	H ₂ O	H ₂ O/H ₂	H ₂ O/H ₂	H ₂ O/H ₂	H ₂ O	H ₂	H ₂	H ₂ O
Pressure (MPa)	6.9	6.8	6.95	0.2	0.2	5–15	0.1	0.1	0.1	0.1
Heating method	Fission	Fission	Fission	Fission	Fission	Decay	Anneal	Anneal	Anneal	Anneal
No. rods/length (m)	32/0.9	32/0.9	28/1.0	20/1.0	20/1.0	36,816/4.0	1/0.2	1/0.2	1/0.08	1/0.08
Krypton, xenon	50	2.6–9.3	23–52	96	77	54	100	100	86	87
Iodine	51	12	24	100	87	55	79	70	87	93
Cesium	32	9	39–51	84	84	55	100	100	93	93
Tellurium	40	1	3	100	83	6	99	82	100	> 98
Barium	1.1	0.6	0.8	1	1		30	76	80	55
Strontium	0.002		0.88			0.1				
Antimony			0.13	62	31	0.16	99	18	97	98
Ruthenium	0.03	0.02	0.007	4	1	0.5	5	0	7	6
Cerium	0.0002	0.009	0.013			0.01				
Europium			0.08			< 0.1				
Zirconium/niobium					< 1					
Molybdenum				No data	56		77	2	47	92
Actinides			< 0.001		< 1					
Zirconium oxidized (%)	75 ^b	28	38 ^b	85	68	45 ^b				
Fuel melted (%)	15	16	18	50	20	45				
Test environment	Steam-rich	Steam	Steam-starved	Steam-rich	Steam-rich	Steam-rich	Steam-rich	Steam-starved	Steam-starved	Steam-rich
Fuel burnup (GWd tU ^{−1})	Trace	Trace	29–42	Fresh	23	3	44	47	38	38

^aTaken from Lewis, B.J., Dickson, R., Iglesias, F.C., Ducros, G., Kudo, T., 2008. J. Nucl. Mater. 380, 126–143.^bTest bundle inventory (core inventory for TMI-2) from Cronenberg, A.W., 1992. Nucl. Technol. 97, 97.

Table 8 Conditions and Ba release data for ORNL (HI and VI) and CEA (HEVA, VERCORS, and VERCORS HT) annealing tests and Phebus tests^a

Test	Temperature (K)	Duration (min)	Atmosphere	Ba release (%)
HI-4	2200	20	H ₂ O	< 1
HI-5	2025	23	H ₂ O	< 1
VI-2	2300	60	H ₂ O	19
VI-3	2700	20	H ₂ O	30
VI-4	2440	20	H ₂	27
VI-5	2720	20	H ₂	76
Heva-4	2270	7	H ₂ O + H ₂	6
Heva-6	2370	30	H ₂	27
Vercors-1	2130	17	H ₂ O + H ₂	4
Vercors-4	2570	30	H ₂	80
Vercors-5	2570	30	H ₂ O	55
Vercors HT-1	3070	7	H ₂	49
Phebus FPT-0	~ 2700	–	H ₂ O/H ₂	1
Phebus FPT-1	~ 2500	–	H ₂ O/H ₂	1

^aTaken from Lewis, B.J., Dickson, R., Iglesias, F.C., Ducros, G., Kudo, T., 2008. J. Nucl. Mater. 380, 126–143.

this difference diminishes afterwards (i.e., above ~2200K), where releases are now dominated by dissolution of the fuel by the molten Zircaloy cladding. Moreover, in [Table 7](#), fuel release is low for the given conditions of the integral experiments and the TMI-2 accident since just a small amount of hydrogen will significantly lower the oxygen partial pressure, thereby affecting the partial pressures of the uranium-bearing vapor species (e.g., UO₃).^{29,128}

With the occurrence of fuel liquefaction, the release of fission products will be governed by atom and bubble migration in the melt. Although this migration mechanism is faster than diffusion in the solid fuel, a release enhancement is not necessarily observed in the integral tests because of the noncoherent nature of the melt progression. As seen in TMI-2, decay heat from the fission products trapped in the ceramic blockage resulted in the formation of a molten pool. The release of fission gases and volatile fission products residing in this molten pool can be further delayed since they must nucleate into bubbles, and then coalesce and grow in the liquid medium by Brownian motion and buoyancy-biased motion, before they can rise to the pool surface for eventual release.¹²⁹ Gas bubbles can also be trapped at the interface between the pool and the crust that surrounds the pool. The oxygen potential of the molten pool will influence the fission product chemical form, that is, the presence of iron oxides in the melt of the TMI-2 establishes a lower limit of about -120 kJ mol^{-1} at 2800K so that fission products such as lanthanum, cerium, and strontium should exist as an oxide (i.e., La₂O₃, Ce₂O₃, or CeO₂, and SrO) that is soluble in the (U, Zr)O₂ ceramic, whereas ruthenium and antimony would be present as metals immiscible in the ceramic melt. Although iodine and cesium are identified as volatile fission products, only small fractions (3%–10%) have been observed in previously molten ceramics in the PBF SFD experiments and the TMI-2 reactor.

2.07.6 Conclusion

The physical chemistry of oxide fuels is an exceedingly daunting technical matter in view of the number of elements and potential phases involved, not to mention the complications of conducting experiments at high temperatures with radioactive systems. Moreover, the elemental composition of the fuel is changing with time and the chemical speciation is influenced by exposure to steam or coolant water in the event of a clad failure or other materials in the case of a reactor accident. Nevertheless, advances by those referenced in computational methodologies rooted in numerical modeling linked to Gibbs energy minimization and related phase field theory are making possible substantial and exciting progress.

See also: 1.27 Computational Kinetics: Application to Nuclear Materials. 2.02 Fuel Performance of Light Water Reactors (Uranium Oxide and MOX). 2.03 Fuel Performance of Fast Spectrum Oxide Fuel. 2.06 Thermal Properties of Irradiated UO₂ and MOX. 2.10 Behavior of LWR Fuel During Loss-of-Coolant Accidents. 2.13 Oxide Fuel Performance Modeling and Simulation. 2.14 Modeling of Pellet Cladding Interaction. 7.03 Thermodynamic and Thermophysical Properties of the Actinide Oxides

References

1. Hocking, W.H., Duclos, A.M., Johnson, L.H., 1994. J. Nucl. Mater. 209, 1–26.
2. Kleykamp, H., 1985. J. Nucl. Mater. 131, 221–246.
3. Cordfunke, E.H.P., Konings, R.J.M., 1988. J. Nucl. Mater. 152, 301–309.
4. Kleykamp, H., 1990. J. Nucl. Mater. 171, 181–188.

5. Kleykamp, H., 1988. Nucl. Technol. 80, 412–422.
6. Bruno, J., Duro, L., Diaz Maurin, F., 2020. Spent nuclear fuel and disposal. In: Piro, M.H.A. (Ed.), *Advances in Nuclear Fuel Chemistry*. Elsevier.
7. DelCul, G.B., Spencer, B., 2020. Reprocessing and recycling. In: Piro, M.H.A. (Ed.), *Advances in Nuclear Fuel Chemistry*. Elsevier.
8. Sah, D.N., Viswanadham, C.S., Kumar, S., Roy, P.R., 1989. Nucl. Technol. 85, 136.
9. Johnson, I., Johnson, C.E., 1988. J. Nucl. Mater. 154, 67–73.
10. Kleykamp, H., 1989. J. Nucl. Mater. 167, 49–63.
11. Cubicciotti, D., Sanecki, J.E., 1978. J. Nucl. Mater. 78, 96.
12. Matzke, H., 1980. J. Radiat. Eff. 53, 219–242.
13. Gittus, J.H., Mathews, J.R., Potter, P.E., 1989. J. Nucl. Mater. 166, 132–159.
14. Ball, R.G.J., Burns, W.G., Henshaw, J., Mignanelli, M.A., Potter, P.E., 1989. J. Nucl. Mater. 167, 191–204.
15. Thompson, W.T., Lewis, B.J., Corcoran, E.C., *et al.*, 2007. Int. J. Mater. Res. 98 (10), 1004–1011.
16. Potter, P.E., 2009. J. Nucl. Mater. 389, 29–44.
17. Kaye, M.H., Lewis, B.J., Thompson, W.T., 2007. J. Nucl. Mater. 366, 8–27.
18. Imoto, S., 1986. J. Nucl. Mater. 140, 19–27.
19. Kleykamp, H., 1979. J. Nucl. Mater. 84, 109–117.
20. Kleykamp, H., 2005. J. Nucl. Mater. 344, 1–7.
21. Kleykamp, H., 1997. J. Nucl. Mater. 248, 209–213.
22. Higgs, J.D., Lewis, B.J., Thompson, W.T., He, Z., 2007. J. Nucl. Mater. 366, 99–128.
23. Arima, T., Masuzumi, T., Furuya, H., Idemitsu, K., Inagaki, Y., 2002. J. Nucl. Mater. 301, 90–97.
24. Sidky, P.S., 1998. J. Nucl. Mater. 256, 1–17.
25. Jacques, P., *et al.*, 1999. J. Nucl. Mater. 264, 239–248.
26. Jacques, P., *et al.*, 1999. J. Nucl. Mater. 264, 249–256.
27. Cronenberg, A.W., Osetek, D.J., 1987. J. Nucl. Mater. 149, 252–260.
28. de Boer, R., Cordfunke, E.H.P., 1997. J. Nucl. Mater. 240, 124–130.
29. Lewis, B.J., Corse, B.J., Thompson, W.T., *et al.*, 1998. J. Nucl. Mater. 252, 235–256.
30. Sunder, S., 2003. Nucl. Technol. 144, 259.
31. Lewis, B.J., Dickson, R., Iglesias, F.C., Ducros, G., Kudo, T., 2008. J. Nucl. Mater. 380, 126–143.
32. Lewis, B.J., Iglesias, F.C., Dickson, R.S., Williams, A., 2009. J. Nucl. Mater. 394, 67–86.
33. Bailly, H., Ménessier, D., Prunier, C., 1999. *The Nuclear Fuel of Pressurized Water Reactors and Fast Reactors: Design and Behaviour*. Paris: Lavoisier, (Commissariat à l’Énergie Atomique).
34. Piro, M.H.A., Sunderland, D., Livingstone, S., *et al.*, 2017. A review of pellet–clad interaction behavior in zirconium alloy fuel cladding. In: Hashmi, Saleen (Ed.), *Reference Module in Materials Science and Materials Engineering*. Oxford: Elsevier, pp. 1–68.
35. Guidez, J., 2016. *Superphénix – Les acquis techniques et scientifiques*. Atlantis Press.
36. Piro, M.H.A., Banfield, J., Clarno, K.T., *et al.*, 2013. Coupled thermochemical, isotopic evolution and heat transfer simulations in highly irradiated UO_2 nuclear fuel. J. Nucl. Mater. 441, 240–251.
37. Kato, M., Komono, A., Uno, H., *et al.*, 2009. J. Nucl. Mater. 393, 134–140.
38. Olander, D.R., 1976. *Fundamental Aspects of Nuclear Reactor Fuel Elements*. TID-26711-P1. Technical Information Centre. US Department of Energy.
39. Nicoll, S., Matzke, H.J., Grimes, R.W., Catlow, C.R., 1997. J. Nucl. Mater. 240, 185–195.
40. Thomas, L.E., Beyer, C.E., Charlot, L.A., 1992. J. Nucl. Mater. 188, 80–89.
41. Manara, D., Seibert, A., Gouder, T., *et al.*, 2020. Experimental methods. In: Piro, M.H.A. (Ed.), *Advances in Nuclear Fuel Chemistry*. Elsevier.
42. Viswanathan, U.K., Sah, D.N., Rath, B.N., Anantharaman, S., 2009. J. Nucl. Mater. 392, 454–551.
43. Une, K., Kashibe, S., 1990. J. Nucl. Sci. Technol. 27, 1002–10016.
44. Small, G.J., 1988. *Proceedings of the IAEA Specialists Meeting on Water Reactor Fuel Element Computer Modelling in Steady State, Transient and Accident Conditions*. Paper IAEA-TC-657/4.3. Preston.
45. Verwerf, M., 2000. Multiple voltage electron probe microanalysis of fission gas bubbles in irradiated nuclear fuel. J. Nucl. Mater. 282, 97–111.
46. Mogensen, M., Bagger, C., 1993. J. Nucl. Mater. 199, 85–101.
47. Matthews, J.R., Small, G.J., 1988. *Proceedings of the IAEA Specialists Meeting on Water Reactor Fuel Element Computer Modelling in Steady State, Transient and Accident Conditions*. Paper IAEA-TC- 657/4.1. Preston.
48. Hiernaut, J.P., Wiss, T., Rondinella, V.V., *et al.*, 2009. J. Nucl. Mater. 392, 34–438.
49. Shirsat, A.N., Ali, M., Kolay, S., Datta, A., Das, D., 2009. J. Nucl. Mater. 392, 16–21.
50. Mansouri, M.A., Olander, D.R., 1998. J. Nucl. Mater. 254, 22–33.
51. Tourasse, M., Boidron, M., Pasquet, B., 1992. J. Nucl. Mater. 188, 49–57.
52. Auvinen, A., Brillant, G., Davidovich, N., *et al.*, 2008. Nucl. Eng. Des. 238, 3418–3428.
53. Iglesias, F.C., Hunt, C.E.L., Garisto, F., Cox, D.S., 1990. *Proceedings of the ICHMT Conference on Fission Products Transport Process in Reactor Accidents*, Dubrovnik, Yugoslavia, May 22–26, 1989. New York: Hemisphere, p. 187.
54. Do, T., Irving, K.G., Hocking, W.H., 2008. J. Nucl. Mater. 383, 34–40.
55. Maeda, K., Sasaki, S., Kato, M., Kihara, Y., 2009. J. Nucl. Mater. 385, 178–183.
56. Rudisill, T.S., 2009. J. Nucl. Mater. 385, 193–195.
57. Baker, L., Just, L.C., 1962. *Studies of Metals Water Reactions at High Temperatures – III Experimental and Theoretical Studies of the Zirconium–water Reaction*. Technical Report ANL-6548 May. Argonne National Laboratory.
58. Duriez, C., Dupont, T., Schmet, B., Enoch, F., 2008. J. Nucl. Mater. 380, 30–45.
59. Piro, M.H.A., 2020. Computational thermochemistry of nuclear fuel. In: Piro, M.H.A. (Ed.), *Advances in Nuclear Fuel Chemistry*. Elsevier.
60. Chevalier, P.Y., Fischer, E., Cheynet, B., 2002. J. Nucl. Mater. 303, 1.
61. Guéneau, C., Dupin, N., Sundman, B., *et al.*, 2011. Thermodynamic modelling of advanced oxide and carbide nuclear fuels: description of the U–Pu–O–C systems. J. Nucl. Mater. 419, 145–167.
62. Lindemer, T.B., Besmann, T.M., 1985. J. Nucl. Mater. 130, 473–488.
63. Blackburn, P.E., 1973. J. Nucl. Mater. 46, 244–252.
64. Eriksson, G., Thompson, W.T., 1989. Calphad 13 (4), 389–400.
65. Kleykamp, H., 1993. J. Nucl. Mater. 206, 82–86.
66. Lyon, W.L., Baily, W.E., 1967. J. Nucl. Mater. 22, 332–339.
67. Kato, M., Morimoto, K., Sugata, H., Konashi, K., Abe, T., 2008. J. Nucl. Mater. 373, 237–245.
68. De Bruycker, F., Boboridis, K., Konings, R.J.M., *et al.*, 2011. On the melting behaviour of uranium/plutonium mixed dioxides with high-Pu content: a laser heating study. J. Nucl. Mater. 419, 186–193.

69. Kleykamp, H., 2001. *J. Nucl. Mater.* 294, 8–12.
70. Philipponeau, T., 1990. Fast Reactor European Collaboration Data Sheet.
71. Belyaev, Y.U.I., 1983. *Radiokhimiya* 25, 791–794.
72. Chikalla, T.D., McNeilly, C.E., Bates, J.L., Rasmussen, J.J., 1971. Proceedings of the International collaboration on the Study of Crystalline Transformation at High Temperature Above 2000K. Odeillo.
73. Kleykamp, H., Paschoal, J.O.A., Pejsa, R., Thümmel, F., 1985. *J. Nucl. Mater.* 130, 426–433.
74. Kleykamp, H., Vincenzini, P. (Eds.), 1987. *High Tech Ceramics*. Amsterdam: Elsevier.
75. Muromara, T., Adachi, T., Takeishi, H., *et al.*, 1988. *J. Nucl. Mater.* 151, 318–326.
76. Prussin, S.G., Olander, D.R., Lau, W.K., Hansson, L., 1988. *J. Nucl. Mater.* 154, 25–37.
77. Lucuta, P.G., Verrall, R.A., Matzke, H.J., Palmer, B.J., 1991. *J. Nucl. Mater.* 178, 48–60.
78. Yamanaka, S., Kurosaki, K., 2003. *J. Alloy. Compd.* 353, 269–273.
79. Teague, M., Gorman, B., Miller, B., King, J., 2014. EBSD and TEM characterization of high burn-up mixed oxide fuel. *J. Nucl. Mater.* 444, 475–480.
80. Kaye, M.H., Thompson, W.T., Lewis, B.J., Sunder, S., O'Connor, R., 2001. Proceedings of the 7th International Conference on CANDU Fuel. Kingston, ON.
81. Imoto, S., 1986. *J. Nucl. Mater.* 140, 19–27.
82. Ewart, F.T., Taylor, R.G., Horspool, J.M., James, G., 1976. *J. Nucl. Mater.* 61, 254–270.
83. Itaki, T., Kono, K., Tachi, H., *et al.*, 1985. *J. At. Energy Soc. Jpn.* 27, 435–449.
84. Chandrasekhariah, M.S., 1985. *J. Nucl. Mater.* 130, 366–374.
85. Kurosaki, K., Uno, M., 1998. *J. Alloy. Compd.* 271–273, 641–644.
86. Cordfunke, E.H.P., Konings, R.J.M., 1990. *Thermochemical Data for Reactor Materials and Fission Products*. Amsterdam: Elsevier.
87. Wang, L.C., 2018. Developing a Thermodynamic Model for the U-Pd-Rh-Ru Quaternary System for Use in the Modelling of Nuclear Fuel. PhD Thesis. Oshawa: University of Ontario Institute of Technology.
88. Oak Ridge National Laboratory, 2005. Radiation Safety Information Computational Center, SCALES–5. Oak Ridge National Laboratory.
89. Walker, C.T., Rondinella, V.V., Papaioannou, D., *et al.*, 2005. On the oxidation state of UO_2 nuclear fuel at a burn-up of around 100 MWd/kgHM. *J. Nucl. Mater.* 345, 192–205.
90. Guéneau, C., Gosse, S., Quaini, A., *et al.*, 2015. FUELBASE, TAF-ID databases and OC software: Advanced computational tools to perform thermodynamic calculations on nuclear fuel materials. In: Proceedings of the 7th European Review Meeting on Severe Accident Research (ERMSAR-2015). Marseille.
91. TAFID, 2018. TAF-ID homepage. Available at: <https://www.oecd-nea.org/science/taf-id>.
92. Kattner, U.R., 2016. The CALPHAD method and its role in material and process development. *Tecnol. Metal. Mater. Min.* 13, 3–15.
93. Lukas, H., Fries, S., Sundman, B., 2007. *Computational thermodynamics: The Calphad method*. Cambridge University Press.
94. Spencer, P., 2008. A brief history of CALPHAD. *Calphad* 32, 1–8.
95. Hillert, M., Jansson, B., Sundman, B., Agren, J., 1985. A two-sublattice model for molten solutions with different tendency for ionization. *Metall. Trans. A* 16, 261–266.
96. Sundman, B., 1991. Modification of the two-sublattice model for liquids. *Calphad* 15(1), 109–119.
97. Lewis, B.J., 1988. *J. Nucl. Mater.* 160, 201–217.
98. Lewis, B.J., MacDonald, R.D., Ivanoff, N.V., Iglesias, F.C., 1993. *Nucl. Technol.* 103, 220–245.
99. Lewis, B.J., El-Jaby, A., Higgs, J., *et al.*, 2007. *J. Nucl. Mater.* 366, 37–51.
100. Killeen, J.C., Turnbull, J.A., 1987. An experimental and theoretical treatment of the release of ^{85}Kr from hyperstoichiometric uranium dioxide. In: Proceedings of the Workshop Chemical Reactivity of Oxide Fuel and Fission Product Release. Gloucestershire, England: Central Electricity Generating Board, p. 387.
101. Cox, D.S., Iglesias, F.C., Hunt, C.E.L., O'Connor, R.F., Barrand, R.D., 1990. High temperature oxidation behaviour of UO_2 in air and steam. In: Proceedings of the International Symposium on High-Temperature Oxidation and Sulphidation Process. Hamilton, ON.
102. Abrefah, J., de Aguiar Braid, A., Wang, W., Khalil, Y., Olander, D.R., 1994. *J. Nucl. Mater.* 208, 98.
103. Lewis, B.J., Duncan, D.B., Phillips, C.R., 1987. *Nucl. Technol.* 77, 303–312.
104. Lewis, B.J., Iglesias, F.C., Postma, A.K., Steininger, D.A., 1997. *J. Nucl. Mater.* 244, 153–167.
105. Bishop, W.N., 1986. Iodine Spiking: EPRI NP-4595. Electric Power Research Institute.
106. Da Silva, R.L., McCracken, D.R., Monserrat, K., 1985. *J. Adv. Ceram.* 17, 107–120.
107. Colle, J.-Y., Hiernaut, J.-P., Wiss, T., *et al.*, 2013. Fission product release and microstructure changes of irradiated MOX fuel at high temperatures. *J. Nucl. Mater.* 442, 330–340.
108. Pourbaix, M., 1966. *Atlas of Electrochemical Equilibria in Aqueous Solutions*. New York: Pergamon.
109. Lewis, B.J., Thompson, W.T., Akbari, F., Morrison, C., Husain, A., 2005. *J. Nucl. Mater.* 340, 69–82.
110. Ticknor, K.V., Cho, Y.H., 1990. *J. Radioanal. Nucl. Chem.* 140, 75–90.
111. Taylor, P., Wood, D.D., Owen, D.G., Park, G.I., 1991. *J. Nucl. Mater.* 183, 105.
112. Piro, M.H., Bruni, G.M.F., Lewis, B.J., *et al.*, 2010. Computation of Actinide Pourbaix Diagrams at 298 K and 550 K ($\text{U,Np,Pu,Am,Cm} - \text{H}_2\text{O}$). In: Proceedings of the 11th International Conference on CANDU Fuel. Niagara Falls, ON.
113. Hobbins, R.R., Petti, D.A., Hargman, D.L., 1993. *Nucl. Technol.* 101, 270.
114. Wright, R.W., Hagen, S.J.L., 1992. In: Krischer, W., Rubinstein, M.C. (Eds.), *The Phebus Fission Product Project*. New York: Elsevier Applied Science, p. 49.
115. Iglesias, F.C., Lewis, B.J., Reid, P.J., Elder, P., 1999. *J. Nucl. Mater.* 270, 21.
116. Konings, R.J.M., Wiss, T., Beneš, O., 2015. Predicting material release during a nuclear reactor accident. *Nat. Mater.* 14, 247–252.
117. Cronenberg, A.W., 1992. *Nucl. Technol.* 97, 97.
118. Dubourg, R., Faure-Geors, H., Nicaise, G., Barrachin, M., 2005. *Nucl. Eng. Des.* 235, 2183–2208.
119. Dubourg, R., Taylor, P., 2001. *J. Nucl. Mater.* 294, 32–38.
120. Hanniet, N., Repetto, G., 1999. Phebus P.F. FPTO – Final Report, CD Version, Suntech 10/99.
121. Allen, M.D., Stockman, H.W., Reil, K.O., Grimley, A.J., Camp, W.J., 1988. ACRR fission product release tests ST-1 and ST-2. In: Proceedings of the International Conference on Thermal Reactor Safety, vol. 5. Avignon.
122. Osborne, M.F., Lorenz, R.A., 1992. *Nucl. Saf.* 33, 344.
123. Andre, B., Ducros, G., Leveque, J.P., *et al.*, 1996. *Nucl. Technol.* 114, 23.
124. Bowsher, B.R., Dickinson, S., Gomme, R.A., *et al.*, 1987. The interaction of zircaloy cladding with fission product tellurium released during a severe reactor accident. In: Proceedings of the Workshop on Chemical Reactivity of Oxide Fuel and Fission Product Release. Berkeley, Gloucestershire: Central Electricity Generating Board, p. 455.
125. De Boer, R., Cordfunke, E.H.P., 1995. *J. Nucl. Mater.* 223, 103.
126. Collins, J.L., Osborne, M.F., Lorenz, R.A., 1987. *Nucl. Technol.* 77, 18.
127. Lewis, B.J., Andre, B., Ducros, G., Maro, D., 1996. *Nucl. Technol.* 116, 34.
128. Olander, D.R., 1999. *J. Nucl. Mater.* 270, 187.
129. McClure, P.R., Leonard, M.T., Razani, A., 1993. *Nucl. Sci. Eng.* 114, 102.